

Oxygen variance and meridional oxygen supply in the Tropical North East Atlantic oxygen minimum zone

J. Hahn · P. Brandt · R. J. Greatbatch ·
G. Krahmann · A. Körtzinger

Received: 29 March 2013 / Accepted: 21 January 2014 / Published online: 14 February 2014
© Springer-Verlag Berlin Heidelberg 2014

Abstract The distribution of the mean oceanic oxygen concentration results from a balance between ventilation and consumption. In the eastern tropical Pacific and Atlantic, this balance creates extended oxygen minimum zones (OMZ) at intermediate depth. Here, we analyze hydrographic and velocity data from shipboard and moored observations, which were taken along the 23°W meridian cutting through the Tropical North East Atlantic (TNEA) OMZ, to study the distribution and generation of oxygen variability. By applying the extended Osborn–Cox model, the respective role of mesoscale stirring and diapycnal mixing in producing enhanced oxygen variability, found at the southern and upper boundary of the OMZ, is quantified. From the well-ventilated equatorial region toward the OMZ core a northward eddy-driven oxygen flux is observed whose divergence corresponds to an oxygen supply of about $2.4 \mu\text{mol kg}^{-1} \text{ year}^{-1}$ at the OMZ core depth. Above the OMZ core, mesoscale eddies act to redistribute low- and high-oxygen waters associated with westward and eastward currents, respectively. Here, absolute values of the local oxygen supply $>10 \mu\text{mol kg}^{-1} \text{ year}^{-1}$ are found, likely balanced by mean zonal advection.

This paper is a contribution to the special issue on tropical Atlantic variability and coupled model climate biases that have been the focus of the recently completed Tropical Atlantic Climate Experiment (TACE), an international CLIVAR program (<http://www.clivar.org/organization/atlantic/tace>). This special issue is coordinated by William Johns, Peter Brandt, and Ping Chang, representatives of the TACE Observations and TACE Modeling and Synthesis working groups.

J. Hahn (✉) · P. Brandt · R. J. Greatbatch · G. Krahmann ·
A. Körtzinger
GEOMAR Helmholtz-Centre for Ocean Research Kiel,
Düsternbrooker Weg 20, 24105 Kiel, Germany
e-mail: jhahn@geomar.de

Combining our results with recent studies, a refined oxygen budget for the TNEA OMZ is derived. Eddy-driven meridional oxygen supply contributes more than 50 % of the supply required to balance the estimated oxygen consumption. The oxygen tendency in the OMZ, as given by the multidecadal oxygen decline, is maximum slightly above the OMZ core and represents a substantial imbalance of the oxygen budget reaching about 20 % of the magnitude of the eddy-driven oxygen supply.

Keywords Oxygen minimum zone · Tropical North East Atlantic · Oxygen variance · Eddy ventilation · Oxygen supply · Oxygen budget

1 Introduction

The oxygen minimum zone (OMZ) of the Tropical North East Atlantic (TNEA) is located south of the subtropical gyre off North West Africa within the shadow zone of the ventilated thermocline (Luyten et al. 1983b). It extends at intermediate depths from 300 to 700 m with a core depth of about 450 m and a meridional core position at about 11°N, where oxygen concentrations of below $40 \mu\text{mol kg}^{-1}$ are frequently observed (Stramma et al. 2009). At depths of about 100 m a second (shallow) oxygen minimum exists, which is separated from the deep oxygen minimum by an intermediate oxygen maximum and whose existence and strength is believed to be more pronounced in the northern part of the OMZ regime (Fischer et al. 2013). Throughout this study, the focus is on the deep oxygen minimum and the shallow oxygen minimum is not discussed further.

The low oxygen content in the OMZ results from the combination of weak mean ventilation and enhanced biological oxygen consumption (Karstensen et al. 2008).

Recent studies have shown that the OMZs of the tropical oceans change in size and oxygen inventory. Stramma et al. (2008b) report an expansion of the TNEA OMZ with a significant average oxygen decrease of $0.34 \pm 0.13 \mu\text{mol kg}^{-1} \text{ year}^{-1}$ over the last decades. Although a model study by Keeling et al. (2010) predicts a decline in the global ocean oxygen inventory of 1–7 % due to anthropogenic forcing, which goes along with an expansion of the OMZs, other studies show that ocean circulation models are in general not yet capable of reproducing the mean shape (Meissner et al. 2005) and the observed trends (Stramma et al. 2012) of the OMZs. A general misrepresentation of the equatorial mean and variable current system at intermediate depth in ocean circulation models is one obvious reason for the failure of those models to correctly represent the observed mean oxygen distribution (Ascani et al. 2010; Brandt et al. 2012; Getzlaff and Dietze 2013). For the explanation of long-term changes in the oxygen distribution of OMZs different mechanisms were suggested involving changes in ventilation and consumption (Bopp et al. 2002; Matear and Hirst 2003; Oschlies et al. 2008; Brandt et al. 2010).

During recent years, mainly in the framework of the collaborative research centre (SFB754) “Climate-Biogeochemistry Interactions in the Tropical Ocean” (2008–2015), several observational studies of hydrographic/circulation mean and variability in the TNEA have been carried out (Stramma et al. 2005, 2008a; Brandt et al. 2008, 2010). Figure 1 in Brandt et al. (2010) shows a map of the horizontal oxygen distribution (at 300–500 m) and the mean currents in the Tropical Atlantic. The most important surface and thermocline currents in the central tropical and subtropical Atlantic are: the North Equatorial Current (NEC) as part of the subtropical gyre circulation, the northern and central branch of the South Equatorial Current (nSEC, cSEC) at 2°N and 4°S , respectively, the North Equatorial Countercurrent (NECC) at 5°N and its northern branch (nNECC) at 9°N , the Equatorial Undercurrent (EUC) as well as the North and South Equatorial Undercurrent (NEUC, SEUC) at 5°N and 5°S , respectively. Below the thermocline, generally weaker currents are found that are part of the equatorial intermediate current system (Ascani et al. 2010; Brandt et al. 2012) including the Equatorial Intermediate Current (EIC) at the equator as well as the Northern and Southern Intermediate Countercurrent (NICC, SICC) at about 2°N and 2°S , respectively.

It was already recognized by Wyrtki (1962) that the shape of an OMZ is determined by the mean current field. In the north, the TNEA OMZ is bordered by the NEC, while in the south, a pronounced equatorial oxygen maximum limits the extension of the OMZ. This maximum is generated by the ventilation due to strong mean and variable zonal currents, where an eastward (westward) flow advects oxygen-rich

(oxygen-poor) waters from (towards) the well-ventilated western boundary (Brandt et al. 2008, 2012). North of the equatorial oxygen maximum in the latitude range of the OMZ, two eastward current bands contribute to the ventilation of the upper OMZ from the west (Stramma et al. 2005). At 4°N – 6°N , the NECC/NEUC band acts as a major source for oxygen-rich South Atlantic Central Water. The nNECC at 8°N – 10°N advects oxygen-rich South Atlantic Central Water as well including an admixture of North Atlantic Central Water (Stramma et al. 2005). Below, in the depth range from 300 to 600 m, the oxygen supply due to mean eastward currents is still present but becomes much weaker.

At the lateral boundaries of an OMZ (or a shadow zone in general), isopycnal eddy fluxes across the boundary play a significant role for its ventilation as discussed analytically (Luyten et al. 1983a) or in numerical models by evaluating the large-scale oxygen budget in OMZs (Gnanadesikan et al. 2013; McCreary et al. 2013). For the equatorial Atlantic, Brandt et al. (2008) argued that meridional eddy fluxes balance zonal advection within an eastward flowing jet along the equator, thus contributing to the ventilation of the off-equatorial regions. Brandt et al. (2010) further followed this hypothesis and show for an idealized mean zonal current system (including the nNECC band as well as the westward flow north and south of it) that in the upper part of the OMZ the diffusive lateral oxygen supply due to eddy fluxes is roughly of the same order of magnitude as the advective oxygen supply due to the mean zonal current system. In particular, the region between the equator and the southern boundary of the OMZ at roughly 5°N is characterized by strong intraseasonal variability associated with Tropical Instability Waves (TIWs) (von Schuckmann et al. 2008) that have been observed in a period band between 25 and 50 days (Athie and Marin 2008) and might contribute to the meridional ventilation of the OMZ.

Apart from the lateral (isopycnal) oxygen supply, Fischer et al. (2013) analyzed diapycnal mixing as a further mechanism for the ventilation of the TNEA OMZ. They estimate the mean oxygen supply due to diapycnal mixing in a depth range between 120 and 570 m and obtain a maximum oxygen supply of about $1.7 \mu\text{mol kg}^{-1} \text{ year}^{-1}$ at about 390 m depth slightly above the core of the OMZ. This value represents a contribution of about one-third to the total oxygen supply required to balance the mean oxygen consumption as estimated by Karstensen et al. (2008). Based on their results, Fischer et al. (2013) defined the isopycnal oxygen supply—either by diffusive or advective fluxes¹—in a residual term, which has not been estimated in an observational study so far. Model-based

¹ Based on their length and time scales we distinguish between lateral fluxes due to mesoscale eddies (diffusive flux) and due to mean currents (advective flux).

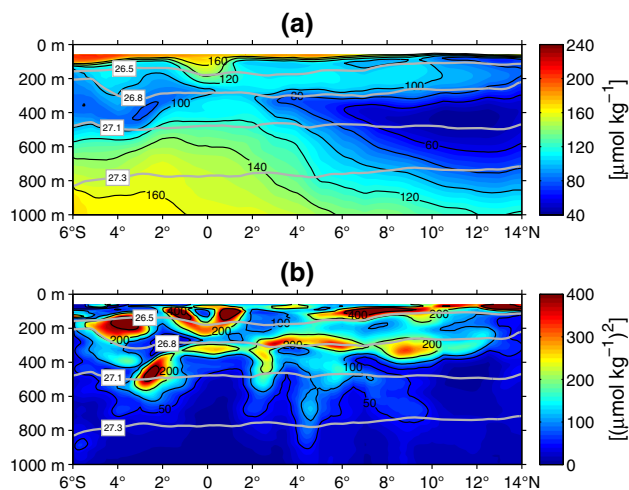


Fig. 1 **a** Mean oxygen concentration and **b** oxygen variance in the Tropical Atlantic along 23°W (color scale and black contours). The analysis was done on isopycnal surfaces and the results were projected back onto depth coordinates. Gray contours mark surfaces of constant potential density

estimates of oxygen budgets in OMZs support these results and find isopycnal eddy fluxes as a dominant ventilation pathway (Gnanadesikan et al. 2013).

Figure 1a, b show meridional sections along 23°W of mean oxygen concentration and oxygen variance, respectively, calculated on density surfaces and projected back onto a depth grid (see Sect. 3.1 for details of the methodology). The analysis on density surfaces removes any effect of isopycnal heaving (due to internal waves or eddies). Furthermore, fluid parcels are strongly constrained to move along isopycnal surfaces (strictly along neutral surfaces) since there is no work done against gravity (McDougall 1987). Thus only changes in water mass properties (e.g. oxygen) on isopycnal surfaces are considered here.² The oxygen variance section shows various maxima indicating strong oxygen variability in the equatorial Atlantic as well as at the boundaries of the OMZ. The southern (5°N–8°N, 400–700 m) and the upper boundary (5°N–12°N, 300 m) of the OMZ are characterized by local oxygen variance maxima. In contrast, the interior of the OMZ shows only weak oxygen variability. Mesoscale eddies, diapycnal mixing as well as zonal current variability are all processes, that might cause this oxygen variability in the Tropical Atlantic.

This study has two major goals. Firstly, we describe the structure of the oxygen variability in the Tropical Atlantic and analyze the different processes contributing to the generation of oxygen variance by applying the extended Osborn–Cox model (Ferrari and Polzin 2005). Secondly,

we estimate the meridional oxygen supply due to eddy fluxes and quantify its contribution to the ventilation of the TNEA OMZ with respect to other terms of the oxygen budget equation. In Sect. 2 we give an overview of the data used within this study. Section 3 describes the methods that are applied. Results are presented in Sect. 4 and discussed in Sect. 5.

2 Data

This study uses hydrographic and velocity data obtained from 3 different sources in order to analyze oxygen variability and meridional eddy-driven oxygen fluxes in the TNEA: (1) repeat ship sections along 23°W (hydrography and velocity), (2) moored observations along 23°W (hydrography and velocity) and (3) climatological data from the World Ocean Atlas 2009. Details of these data sets are described in the following.

2.1 Velocity and hydrographic data obtained from repeat ship sections along 23°W

Velocity and hydrographic data along the 23°W section were obtained during several research cruises in the Tropical Atlantic carried out from 1999 to 2011 (see Table 1 for details). Velocity data were acquired with vessel-mounted (vm-ADCP) and lowered ADCPs (l-ADCP); hydrographic data with a CTD/O₂ probe. Data records were taken into account from 22°W to 24°W and 6°S to 14°N. The narrow zonal extent that was chosen here was necessary to accurately estimate the local variability of hydrographic properties along 23°W as a function of latitude.

Measurement errors for velocity and hydrographic data are the same as described in Brandt et al. (2010), who analyzed a similar data set that was based on ship sections taken between 22°W and 29°W in the period 1999–2008. For a single research cruise the accuracy of 1-h averaged velocity data from vm-ADCP and single velocity profiles from l-ADCP was better than 2–4 and 5 cm s^{−1}, respectively. By averaging all individual velocity sections the mean velocity was estimated with an average standard error of about 1.8 cm s^{−1} for the meridional range between 6°S and 14°N and the depth range 100–1,000 m. The accuracy of hydrographic data was 0.001 °C, 0.002 and 2 μmol kg^{−1} for temperature, salinity and dissolved oxygen, respectively.

2.2 Moored observations along 23°W

Along the 23°W meridian, we performed hydrographic measurements with moorings located at the equator, 2°N,

² Note, oceanic biogeochemistry and ecosystems might be diversely affected by oxygen variability both in depth and density space.

Table 1 Meridional shipboard ADCP and CTD/O₂ sections between 6°S–14°N and 22°W–24°W

Cruise (date)	VM-ADCP/L-ADCP		CTD/O ₂		
	Latitude/longitude	Depth (m)	Latitude/longitude	Depth (m)	# Profiles
Thalassa (July–August 1999)	6°S–6°N/23°W	1,000	6°S–6°N/23.1°W–22.5°W	1,000	45
Seward Johnson (January 2000)	6°S–4°N/23°W	1,000	–	–	–
Meteor 47/1 (April 2000)	5°S–4°N/23°W	1,000	5°S–4°N/24.0°W–23.0°W	1,000	27
Meteor 55 (October 2002)	0°–10°N/24°W	650	–	–	–
Polarstern Ant XXII/5 (June 2005)	6°S–14°N/23°W	300	–	–	–
Meteor 68/1 (May 2006)	2°S–0.5°N/23°W	500	–	–	–
Ron Brown (June 2006)	5°S–13.5°N/23°W	750	5°S–14°N/23.0°W	1,000	96
	5°S–14°N/23°W	750			
Meteor 68/2 (June–July 2006)	4°S–14°N/23°W	1,000	4°S–14°N/23.2°W–22.0°W	1,000	48
Ron Brown 2007 (May 2007)	4°N–14°N/23°W	750	4°N–14°N/23.1°W–22.6°W	1,000	22
L'Atalante (February–March 2008)	2°S–14°N/23°W	400	2°S–14°N/23.1°W–23.0°W	1,000	48
	2°S–14°N/23°W	1,000			
Merian 08/1 (April–May 2008)	7.5°N–14°N/23°W	600	7°N–11°N/24.0°W–22.0°W	1,000	36
Merian 10/1 (November–December 2008)	4°N–14°N/23°W	650	4°N–14°N/24.0°W–22.0°W	1,000	70
Polarstern Ant XXV/5 (May 2009)	6°S–14°N/23°W	250	–	–	–
Endeavor 463 (May–June 2009)	4°S–3°N/23°W	700	–	–	–
Ron Brown (July–August 2009)	0°–14°N/23°W	700	–	–	–
Polarstern Ant XXVI/1 (November 2009)	6°S–14°N/23°W	250	–	–	–
Meteor 80/1 (October–November 2009)	5°S(6°S)–14°N/23°W	1,000 (590)	5°S–14°N/23.1°W–23.0°W	1,000	76
	6°S–14°N/23°W	600			
Meteor 80/2 (December 2009)	–	–	4°N–11°N/24.0°W–22.0°W	1,000	9
Meteor 81/1 (February–March 2010)	6°S–13°N/22°W	1,000	–	–	–
Polarstern Ant XXVI/4 (May 2010)	5°S–13.5°N/23°W	250	–	–	–
Meteor 83/1 (October–November 2010)	–	–	2°N–14°N/24.0°W–22.0°W	1,000	21
MSM18/2 (May–June 2011)	0°–14°N/23°W	1,000	5°S–5°N/23.0°W	1,000	29
	5°S–5°N/23°W	1,000			
Ron Brown (July–August 2011)	0°–12.2°N (14°N)/23°W	700 (650)	–	–	–

Latitude/longitude and depth of each section mark the latitude and longitude range as well as the maximum depth of the used data. # Profiles marks the number of CTD/O₂ profiles that were available from this cruise and were used for our analysis. A dash signifies that no velocity or CTD/O₂ data was used from this cruise

5°N and 8°N (see Table 2 for details). Oxygen sensors (AADI Aanderaa optodes of model types 3830 and 4330) and CTD sensors (Sea-Bird microcats) were attached next to each other on the mooring cable to allow the interpolation of the measured oxygen onto density surfaces (Fig. 2). Overall, we recorded oxygen time series at the equator and 2°N at depths of 300 and 500 m. At 5°N and 8°N, oxygen time series were obtained at depths from 100 to 800 m with eight evenly distributed optode/microcat combinations per mooring. The sampling rate for all instruments was set to 2 h or better. During the mooring period March 2008–October 2009, the two optodes in the equatorial mooring only worked for about 2 weeks due to a too high power consumption. During the mooring period May 2011–October 2012, one optode (200 m) of the 5°N mooring only worked for about 4 months and the logger electronics of another optode (700 m) was missing at

recovery likely because of a pressure housing failure. All other optodes worked properly over their whole mooring period. Two microcats failed completely and three microcats developed corrupt conductivity cells, so only a fraction of the salinity data was usable for these instruments. In case of missing microcat data, we used the optode temperature and estimated the salinity by applying a mean θ – S relation (θ being the potential temperature) obtained from water mass properties at nearby CTD measurements.

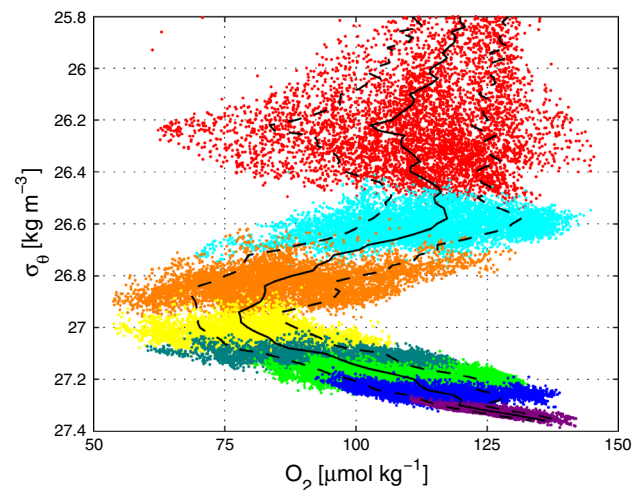
All optodes were calibrated before and after the mooring deployment both in the field and in the laboratory onboard. Every optode was attached to the CTD rosette and calibrated against oxygen measurements of a CTD/SBE 43 Clark electrode (which itself was calibrated against Winkler titrated water samples) that were taken during several minute long stops of a regular CTD/O₂ cast in order to allow an equilibration of the optode oxygen sensors.

Table 2 CTD and oxygen sensors deployed during different mooring periods and at different depths along 23°W (equator, 2°N, 5°N and 8°N)

Position (date)	Depth (m)	S (%)	T (%)	O ₂ (%)
0°N, 23°W (March 2008–October 2009)	300	×	×	2
	500	×	×	2
0°N, 23°W (November 2009–May 2011)	300	×	×	×
	500	×	×	×
2°N, 23°W (March 2008–October 2009)	300	×	×	×
	500	×	×	×
5°N, 23°W (November 2009–May 2011)	100	×	×	×
	200	×	×	×
	300	×	×	×
	400	×	×	×
	500	×	×	×
	600	×	×	×
5°N, 23°W (May 2011–October 2012)	700	×	×	×
	800	0	×	×
	100	×	×	×
	200	×	×	24
	300	×	×	×
	400	×	×	×
	500	×	×	×
	600	×	×	×
8°N, 23°W (November 2009–May 2011)	700	×	×	0
	800	×	×	×
	100	×	×	×
	200	×	×	×
	300	×	×	×
	400	×	×	×
	500	×	×	×
	600	0	×	×
8°N, 23°W (May 2011–October 2012)	700	41	×	×
	800	×	×	×
	100	×	×	×
	200	×	×	×
	300	×	×	×
	400	×	×	×
	500	×	×	×
	600	28	×	×
	700	×	×	×
	800	96	×	×

The quality of salinity (S), temperature (T) and oxygen (O₂) time series is shown. A cross marks a clean record (100 % good data) of the instrument. Percentages signify the rate of good data referred to total mooring time period

Additionally, an onboard lab calibration was performed by submerging every optode into a sodium sulfite solution (5 g Na₂SO₃ per 500 ml as recommended by the optode manufacturer) with zero oxygen content.

**Fig. 2** Oxygen concentration as a function of potential density as obtained from moored observations at 5°N, 23°W (November 2009–May 2011). Different colors mark instruments located at different depths between 100 and 800 m (see Table 2 for details). Mean and standard deviation are shown as solid and dashed lines, respectively

Based on all in situ and lab reference points, we conducted one comprehensive calibration for every optode using the following algorithm. We applied the general optode foil characteristics, as described in Uchida et al. (2008), to calculate the dissolved oxygen from temperature and the optode phase signal. The calibration against reference oxygen samples was done by linearly correcting the raw phase signals of the optode output with temperature and raw phase itself before applying the Uchida et al. (2008) formula. A pressure correction was done as described in the manuals for type 3830 (AADI 2007) and type 4330 (AADI 2009) with a correction factor of 0.04/1,000 dbar. Finally, the salinity correction for dissolved oxygen in seawater after Garcia and Gordon (1992) was applied. From the misfit against CTD/O₂ and lab calibration points, we estimated the root mean square error of the oxygen sensors to be in the range from 1.5 to 4.5 μmol kg⁻¹ (average error <3 μmol kg⁻¹).

Sea-Bird microcats were calibrated before and after the mooring deployment by attaching them to the CTD rosette. Temperature, conductivity and pressure sensors were linearly calibrated against temperature, conductivity and pressure, respectively, of the Sea-Bird CTD sensor. Only data from selected several minute long stops were used for the calibration in order to allow the relatively slow sensors to equilibrate.

Horizontal velocity was measured at the mooring positions 5°N, 23°W and 8°N, 23°W during different mooring periods (see Table 3 for details) with downward or upward looking 75-kHz Longranger ADCPs. The sampling period and bin length was set to 2 h and 16 m, respectively. The minimum measurement range was from 100 to 750 m such

Table 3 ADCPs that were deployed at 5°N, 23°W and 8°N, 23°W during different mooring periods

Position (date)	ADCP depth range (m)
5°N, 23°W (July 2006–February 2008)	70–750
5°N, 23°W (November 2009–May 2011)	100–780
5°N, 23°W (May 2011–October 2012)	60–750
8°N, 23°W (May 2011–October 2012)	60–750

Depth ranges for velocity measurements are shown

that the depths of almost all optodes were covered. An ensemble number of 20 pings were chosen, which resulted in a standard error of 1.7 cm s^{-1} for a single velocity data point. Following the manufacturer's compass accuracy of about 2° we inferred a velocity error of $<4\%$ of the absolute measured velocity.

2.3 Climatological data: World Ocean Atlas 2009

Most of the considered shipboard CTD/ O_2 surveys followed the 23°W section (see Table 1). These observations do not provide sufficient information on the hydrographic properties in zonal direction. Hence, for our analyses we additionally used the annual climatological data from the World Ocean Atlas 2009 [WOA09, available at http://www.nodc.noaa.gov/OC5/WOA09/pr_woa09.html, described in Locarnini et al. (2010), Antonov et al. (2010), Garcia et al. (2010)], and calculated mean salinity and oxygen distributions on potential density surfaces for the Tropical Atlantic.

3 Methods

This study is mainly aimed at the quantitative description of the oxygen variability and the meridional oxygen flux due to mesoscale eddies. The analysis is based on both a diffusive flux parameterization by using a lateral eddy diffusion coefficient (Sects. 3.4, 3.5) and a flux correlation (Sect. 3.5). The determination of a reliable lateral eddy-diffusion coefficient is a long-standing challenge in oceanography and different methods have been applied in various studies to estimate eddy diffusivities from observational (Ferrari and Polzin 2005; Funk et al. 2009) or model data (Gent and McWilliams 1990; Eden and Greatbatch 2009; Kamenkovich et al. 2009). However, the estimate of the eddy diffusivity is often accompanied by large uncertainties, hence, the estimate of material fluxes using a diffusive flux parameterization has to be considered with care. The flux correlation is an alternative method, but long time series are needed to arrive at results with high significance. In this study, both methods are applied and

are discussed in detail to test the reliability of these estimates.

Section 3.1 describes the estimates of the hydrographic/velocity mean and variance sections from shipboard and moored observations. In Sect. 3.2, the methodology to estimate the characteristic eddy velocity needed for the eddy diffusivity parameterization is presented. Section 3.3 introduces two approaches to derive the eddy diffusivity by including the methods from 3.1 and 3.2. In Sect. 3.4, we show the estimate of the oxygen variance production terms based on the extended Osborn–Cox model in order to identify the respective role of mesoscale eddies and diapycnal mixing in generating enhanced oxygen variability. Finally, Sect. 3.5 describes (1) two methods for the estimate of the meridional oxygen flux, (2) the spectral analysis of the meridional oxygen flux to identify dominant time scales, and (3) a method to estimate the eddy-driven meridional oxygen supply as well as the oxygen budget for the TNEA.

3.1 Mean and variance sections along 23°W

In this section shipboard and moored observations are used to estimate the hydrographic/velocity mean fields and their variability in the Tropical Atlantic along 23°W. The analysis is the basis for the quantification of the characteristic eddy velocity (Sect. 3.2), the eddy diffusion coefficient (Sect. 3.3), the variance-generating processes (Sect. 3.4) and eventually the eddy-driven meridional oxygen flux and supply (Sect. 3.5) along 23°W.

Based on the hydrographic ship sections, the meridional mean and variance sections of salinity and oxygen (along 23°W) were calculated with respect to potential density surfaces (oxygen shown in Fig. 1; salinity not shown). The calculation was carried out as follows: single CTD/ O_2 profiles in a zonal range between 22°W and 24°W were assembled to a hydrographic data set as a function of potential density σ_θ and latitude ϕ , where the i th CTD/ O_2 profile of a hydrographic tracer C (salinity or dissolved oxygen) is defined as $C_i = C_i(\sigma_\theta, \phi_i)$. Mean and variance of C were then calculated as weighted variables using a two-dimensional Gaussian interpolation scheme:³

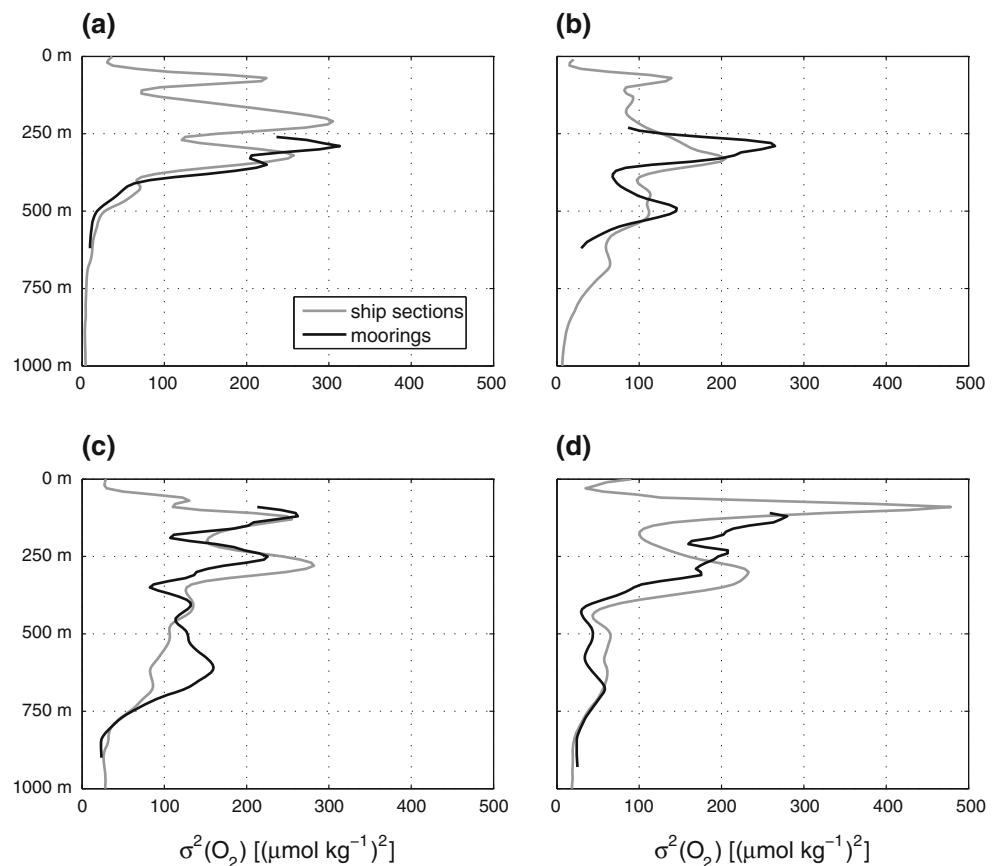
$$\bar{C}(\sigma_\theta, \phi) = \frac{\sum_i w_i C_i}{\sum_i w_i} \quad (1)$$

$$\sigma_C^2(\sigma_\theta, \phi) = \frac{\sum_i w_i (C_i - \bar{C})^2}{\sum_i w_i} \quad (2)$$

where $\bar{C}(\sigma_\theta, \phi)$ is the weighted mean and $\sigma_C^2(\sigma_\theta, \phi)$ is the weighted variance. The (Gaussian) weights w_i were

³ Strictly speaking, in isopycnal coordinates these would be thickness-weighted means (De Szoeke and Bennett 1993).

Fig. 3 Oxygen variance as a function of depth obtained from repeat shipboard CTD/O₂ sections (*gray line*) and moored observations (*black line*) for the latitudes. **a** 0°, **b** 2°N, **c** 5°N, and **d** 8°N along 23°W (see Tables 1, 2 for details of used data)



determined with the meridional and diapycnal influence (cutoff) radii 0.5° (1.0°) and ~ 0.01 – 0.1 kg m^{-3} (~ 0.02 – 0.2 kg m^{-3}) with maximum diapycnal radii at the surface and minimum at depth. The procedure allowed a determination of mean and variance of C on isopycnal surfaces, i.e. the resulting tracer variability was unaffected by vertical movements of isopycnal surfaces. Due to the large number of CTD/O₂-profiles, the fields $\bar{C}(\sigma_\theta, \phi)$ and $\sigma_C^2(\sigma_\theta, \phi)$ could be obtained at a meridional resolution of 0.5° , so that regional differences particularly in oxygen variability were resolved. Subsequently, the fields were transformed back onto depth coordinates by using the mean depth of the density surfaces $\bar{z}(\sigma_\theta, \phi)$, which was estimated from the mean hydrographic section. Due to high depth variability of near surface density layers, we did not perform this calculation in the upper 60 m.

The CTD/O₂ data used for this analysis had a very sparse time resolution. Hence, we additionally estimated the oxygen variance from mooring time series at the equator, 2°N, 5°N and 8°N along 23°W. As an example, Fig. 2 shows oxygen as a function of potential density recorded from the 5°N, 23°W mooring during the period November 2009–May 2011. Although oxygen was measured on eight distinct depth levels ($\Delta h = 100 \text{ m}$), a quasi-continuous record of oxygen over potential densities from $\sigma_\theta = 26.3$ to

$\sigma_\theta = 27.3 \text{ kg m}^{-3}$ was derived due to the vertical displacement of isopycnal surfaces. Mean and standard deviation of oxygen were derived as a function of potential density and are shown as black solid and dashed lines, respectively. Obvious is the clear oxygen minimum at the potential density surface $\sigma_\theta = 27.0 \text{ kg m}^{-3}$. For all four mooring positions oxygen variance profiles were estimated and, similar to the 23°W oxygen variance section (Fig. 1b), these profiles were projected back onto depth grid by applying a mean depth for every density surface (Fig. 3).

In order to determine a velocity section along 23°W, the ADCP data were processed as described in Brandt et al. (2010), i.e. vm-ADCP/I-ADCP data were merged and meridional sections were determined on a regular grid (vertical resolution: $dz = 10 \text{ m}$; meridional resolution $d\phi = 0.05^\circ$) for each single ship section. Based on all meridional sections, we calculated the mean and the variability (standard deviation) of zonal and meridional velocity (\bar{u} , \bar{v} , σ_u , σ_v) for a depth range and a meridional range of 100–1,000 m and 6°S – 14°N , respectively (mean zonal velocity is shown in Fig. 4a). Henceforth, we refer to it as the 23°W velocity section. The average standard error of the mean velocity was estimated to be 2.1 and 1.6 cm s^{-1} for the equatorial regime (6°S – 4°N) and for the meridional range 4°N – 14°N , respectively.

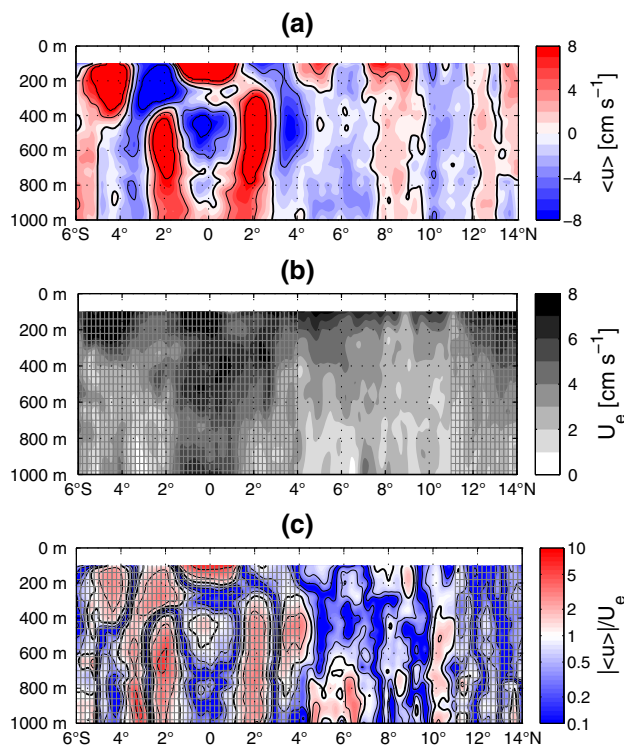


Fig. 4 **a** Mean zonal velocity, **b** characteristic eddy velocity U_e and **c** ratio of absolute mean zonal velocity over characteristic eddy velocity along 23°W. In **a** thick solid line marks 0 cm s⁻¹ and thin solid lines mark isolines -8, -4, 4 and 8 cm s⁻¹, respectively. In **c** thick solid line marks isoline 1, thin solid lines mark isolines 0.2, 0.5 and 2, 5, respectively. Hatched areas in **b** and **c** mark regions, where U_e is uncertain and that are not used for further analysis

3.2 Characteristic eddy velocity

In the following section the derivation of the characteristic eddy velocity that is based on shipboard and moored observations carried out along 23°W (cf. Sects. 2.1, 2.2) is presented. It is required to estimate the lateral eddy diffusion coefficient (Sect. 3.3).

The characteristic velocity U_e of mesoscale eddies is defined as the square root of the eddy kinetic energy

$$U_e = \sqrt{\frac{u_e^2 + v_e^2}{2}} \quad (3)$$

where u_e and v_e represent the magnitude of zonal and meridional velocity fluctuations according to the mesoscale eddy field. A suitable method to derive these fluctuations is the analysis of mesoscale variability from velocity time series (Müller and Siedler 1992). Here, we used velocity time series recorded during the three mooring periods at 5°N, 23°W (cf. Table 3).

The observed velocity fluctuations contain contributions from the mesoscale eddy field as well as from inertial and tidal variability. By definition, near-inertial and tidal oscillations are not part of the velocity variability on the

mesoscale and hence have to be excluded in the calculation of u_e and v_e . Near-inertial and tidal oscillations were removed by applying a low-pass filter to the time series, i.e. $Lu = L \times u$ and $Lv = L \times v$ with the low-pass filter operator⁴ $L = L(1/f_c)$ and the cutoff frequency f_c , which was chosen corresponding to a period of 10 days (the inertial period is $T_i = 5.7$ days at 5°N). Finally, u_e and v_e were calculated as the standard deviation of the low-pass filtered time series (σ_{Lu} and σ_{Lv}).

The estimate of the characteristic eddy velocity U_e from mooring time series as described above is limited to a single mooring position. To estimate U_e for a broad latitudinal range, we used the standard deviations σ_u , σ_v of the 23°W velocity section estimated from repeated ship sections (Sect. 3.1). In contrast to mooring time series, repeated shipboard measurements do not include a similar time resolution to spectrally split these velocity fluctuations in order to obtain the characteristic eddy velocity. Alternatively, we used the 5°N, 23°W mooring velocity time series to configure a parameterization for the low-pass filter L as described in the Appendix 1. We applied this parameterization [Eqs. (19), (20)] on σ_u and σ_v to estimate the velocity variability on the mesoscale (cf. Fig. 5). Here the estimated u_e and v_e are considered as ensemble mean values [cf. Lilly et al. (2003)]. We finally calculated a meridional section of the characteristic eddy velocity U_e (cf. Fig. 4b) using (3). As will be shown in Sect. 4.2, U_e was assumed to be valid between 4°N and 11°N.

3.3 Eddy diffusivity

One way to represent the along-isopycnal tracer flux is to parameterize it as a diffusive flux⁵ that is along the mean isopycnals and down the mean isopycnal tracer gradient. The methodology for doing this is described in detail in Ferrari and Polzin (2005) and ultimately rests on the idea that in a statistically steady state, production of tracer variance is balanced by dissipation (ultimately, molecular dissipation in the ocean interior), as in the traditional Osborn–Cox model (Osborn and Cox 1972). Eden et al. (2007) and Eden et al. (2009) have shown how the original Osborn–Cox model can be extended to account for spatial inhomogeneity, in which case the advective fluxes of tracer

⁴ Here a butterworth filter of 3rd order was used.

⁵ In one dimensional case (here meridional), this is $\overline{v'C'} \approx K_e \nabla_y \bar{C}$ with meridional velocity v , tracer C , eddy diffusivity K_e , the meridional derivative ∇_y and overbar denotes the spatial and temporal average of the fluctuations. The parameterization into a diffusive flux and, in turn, the parameterization of an eddy diffusivity considers the following assumptions (Vallis 2006). (1) The mean tracer gradient varies on a spatial scale that is large compared to the mixing length [cf. (5)] of the tracer. (2) The tracer is a conserved quantity and it is able to be mixed with its surroundings.

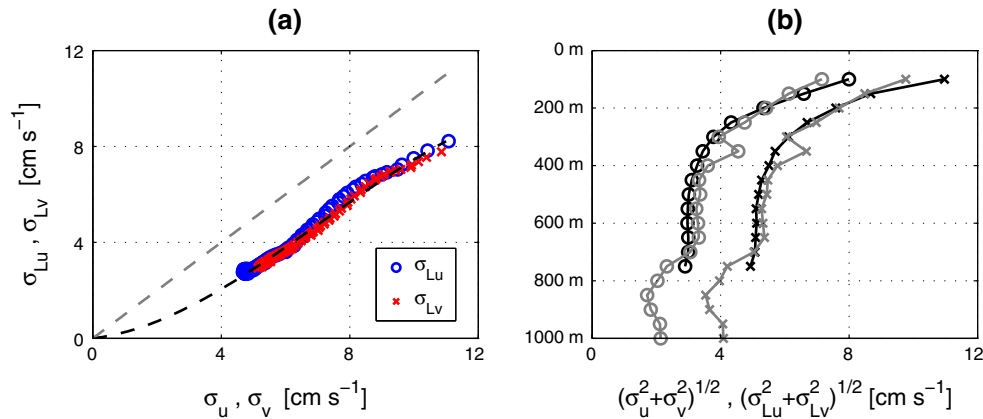


Fig. 5 **a** Standard deviation of low-pass filtered velocity (σ_{Lu} , σ_{Lv}) versus standard deviation of unfiltered velocity (σ_u , σ_v) obtained from the 5°N, 23°W mooring velocity data. *Blue circles* and *red crosses* mark the estimates from the zonal and the meridional component, respectively. The *black dashed line* is the parameterization function (see text for details) and the *gray dashed line* marks the bisection line, i.e. $\sigma_{Lu} = \sigma_u$. **b** Velocity variability as a function of depth at

5°N, 23°W. *Black* (mooring data) and *gray* (ship section data) line with *crosses* mark the calculation using the unfiltered velocity, i.e. $\sqrt{\sigma_u^2 + \sigma_v^2}$. *Black* (mooring data) and *gray* (ship section data) line with *circles* mark the calculation using the low-pass filtered velocity, i.e. $U_e = \sqrt{\sigma_{Lu}^2 + \sigma_{Lv}^2}$, representing the characteristic eddy velocity

variance are largely balanced by rotational tracer fluxes [see also Eden and Greatbatch (2009)].

In order to evaluate the diffusive flux parameterization in Sects. 3.4 and 3.5, the eddy diffusivity K_e for the TNEA has to be quantified. To estimate K_e , we applied two different approaches (in the following introduced as $K_e^{(1)}$ and $K_e^{(2)}$) since one approach alone was found to be not capable of estimating K_e for the whole depth range of 100–1,000 m.

The first parameterization is based on the mixing length theory and was already used in Ferrari and Polzin (2005). The eddy diffusivity is given by

$$K_e^{(1)} = c_e U_e L_e \quad (4)$$

L_e is the mixing length and defines the distance that a fluid particle can move on an isopycnal surface before interchanging its properties with the surrounding fluid. From observations the mixing length can be estimated as

$$L_e = \frac{\sigma_C}{|\nabla_\sigma C_m|}, \quad (5)$$

where σ_C represents the local tracer fluctuation on the isopycnal surface σ_θ with the mean tracer gradient $\nabla_\sigma C_m$. We estimated σ_C from the square root of the tracer variance (using both salinity and oxygen) as obtained from (2). The absolute value of the mean isopycnal tracer gradient is calculated as the modulus of the mean zonal and the mean meridional isopycnal gradient

$$|\nabla_\sigma C_m| = \sqrt{(\nabla_{\sigma x} C_m)^2 + (\nabla_{\sigma y} C_m)^2}, \quad (6)$$

$\nabla_{\sigma y} C_m$ is determined using the mean hydrographic 23°W section calculated by (1). Since no hydrographic

information in the zonal direction can be obtained from the mostly meridionally aligned measurements, the mean zonal isopycnal tracer gradient $\nabla_{\sigma x} C_m$ is calculated from the hydrographic mean fields (temperature, salinity, oxygen) of the World Ocean Atlas 2009. It is found that $\nabla_{\sigma y} C_m$ dominates at latitudes close to the southern boundary of the OMZ (5–10 times larger than $\nabla_{\sigma x} C_m$), whereas both gradients are of comparable order of magnitude close to the OMZ core latitudes (it is, therefore, reasonable to take $\nabla_{\sigma x} C_m$ into account).

U_e is the characteristic velocity of the mesoscale given by (3) and c_e is an efficiency factor, that describes the mixing efficiency of mesoscale turbulence. For the mixing efficiency we use the same value ($c_e = 0.16$) as was used by Ferrari and Polzin (2005), who refer to an observational study by Wunsch (1999). It is considered as an average global value for the mixing efficiency of mesoscale eddies.

For the calculation of the mixing length L_e in (5) we have to assume that almost all tracer fluctuations on an isopycnal surface are generated by mesoscale turbulence–diapycnal mixing has to be negligible.⁶ Thus, the mixing length can only be estimated for locations with a strong mean isopycnal and a weak mean diapycnal tracer gradient. Otherwise, a contribution of diapycnal mixing to the tracer variance would result in an overestimation of L_e . To estimate its validity, we determined L_e based on two independent tracers: salinity and oxygen. That is, mixing lengths L_e^S (based on salinity) and L_e^O (based on oxygen) are calculated and compared to each other. We propose L_e as

⁶ Here, we refer to the two variance-generating processes (mesoscale stirring and diapycnal mixing) as considered in the extended Osborn–Cox model in (11).

properly determined in regions with a large mean isopycnal tracer gradient and if the condition $L_e^S \approx L_e^O$ is valid over length scales much larger than the mixing length itself. Regions, where the estimated mixing length L_e is trustworthy, are discussed in the end of this section.

The second parameterization of the eddy diffusivity that was analyzed in Eden and Greatbatch (2008) is given by

$$K_e^{(2)} \sim U_e L_R, \quad (7)$$

U_e is again the characteristic velocity of the mesoscale determined by (3). L_R is the Rhines scale, which is a better approximation for the eddy length scale in the Tropical and Subtropical Atlantic (<30°N) than the local Rossby radius (Eden 2007). In Eden (2007) the Rhines scale is defined by

$$L_R = \sqrt{\frac{U_e}{2\beta}} \quad (8)$$

It characterizes the length scale of two-dimensional mesoscale turbulence on a β -plane. For the Tropical and Subtropical Atlantic, Eden (2007) and Eden and Greatbatch (2009) show an anisotropy of the eddy length scale and the eddy diffusivity. This anisotropy is due to the β -effect that results in an inverse energy cascade from wavenumbers corresponding to mesoscale eddies and leads to zonally elongated eddies and time mean zonal currents. In a model-based study on zonal and meridional spreading rates in the North Atlantic Kamenkovich et al. (2009) describe a superdiffusive character in the zonal direction, whereas mesoscale eddies have a purely diffusive effect in the meridional direction. However, from the analysis of our moored and shipboard observations we found an almost isotropic distribution of zonal and meridional velocity variability⁷ on the mesoscale (not shown) and we assume that our estimate of the eddy diffusivity represents the diffusive character of the eddy field without any parameterization of eddy-driven mean zonal jets. Combining (7) and (8) yields proportionality between eddy diffusivity and characteristic eddy velocity to the power of 3/2 with a weak latitudinal dependence due to β :

$$K_e^{(2)} \sim \sqrt{\frac{U_e^3}{2\beta}} \quad (9)$$

Eden (2007) noted that no uniform definition for the Rhines scale exists [cf. Eden and Greatbatch (2008)], that mainly results from the definition of the characteristic velocity, which could be defined either by barotropic, first baroclinic mode or local velocity fluctuations.⁸ Thus, we

introduce a constant scaling factor α (which still has to be determined) such that

$$K_e^{(2)} = \alpha \sqrt{\frac{U_e^3}{2\beta}} \quad (10)$$

The two parameterizations (4) and (10) have the following restrictions. For $K_e^{(2)}$ the scaling factor α needs to be determined. $K_e^{(1)}$ can only be determined for regions with a well-defined mixing length L_e , i.e. where a strong mean isopycnal tracer gradient exists. Once a reasonable $K_e^{(1)}$ is estimated for such a region we can fit $K_e^{(2)}$ to $K_e^{(1)}$ in order to determine the constant scaling factor α , which finally allows an estimation of $K_e^{(2)}$ independent from L_e . Both parameterizations are a function of the characteristic eddy velocity U_e . Hence, the estimation of K_e depends on the validity of U_e , as discussed further in Sect. 4.2.

In summary, our approach to determine the eddy diffusivity was the following:

1. We estimated the eddy length scale L_e by applying (5) for salinity and oxygen from shipboard CTD/O₂ sections (not shown). By comparing the results of the mixing lengths L_e^S and L_e^O we checked the robustness of the calculation. We found a good correspondence of both mixing lengths for the latitudes 4°N–10°N and for a depth range of 450–800 m with an average length scale of about $L_e = 100$ km. This region is characterized by strong (meridional) gradients both in salinity (transition zone from South Atlantic Central/Intermediate Water to North Atlantic Central/Intermediate Water) and oxygen (transition zone from the well-ventilated equatorial region to the core of the TNEA OMZ).
2. We used (4) to determine the eddy diffusivity $K_e^{(1)}$ based on the eddy length scale L_e estimated in (5) and on the characteristic eddy velocity U_e in (3). Restricted by both L_e and U_e we found a reasonable estimate for $K_e^{(1)}$ in the latitudinal range 4°N–10°N and for the depth range 450–800 m. According to Ferrari and Polzin (2005) we assumed the error for $K_e^{(1)}$ with a factor 2, i.e. $[0.5 K_e^{(1)}, 2 K_e^{(1)}]$.
3. We determined the scaling factor α in (10) by fitting $\sqrt{U_e^3/2\beta}$ to the eddy diffusivity $K_e^{(1)}$ for the latitudes 4°N–6°N in the depth range 450–800 m and found $\alpha = 0.59$. Using this scaling factor, $K_e^{(2)}$ was calculated between 4°N and 11°N (meridionally restricted again by U_e) and over a depth range from 100 to 1,000 m.
4. As for $K_e^{(1)}$ the uncertainty of $K_e^{(2)}$ was assumed with a factor 2. We found that the meridional variability of $K_e^{(2)}$ between 4°N and 11°N is smaller than its uncertainty. Hence, we determined one mean eddy diffusivity profile

⁷ With a slight tendency to enhanced meridional velocity fluctuations.

⁸ Within this study we estimated U_e based on the local velocity fluctuations as given by (3).

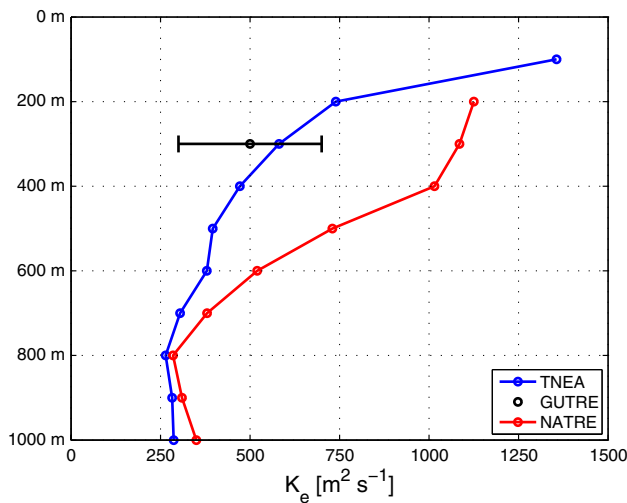


Fig. 6 Depth profile of the eddy diffusivity. Blue line marks our estimate for the Tropical North East Atlantic (4°N–11°N, 23°W). Black dot with error bar marks the eddy diffusivity from the Guinea Upwelling Tracer Release Experiment (GUTRE) at 8°N, 23°W (Banyte et al. 2013) and the red line marks the eddy diffusivity estimated from data acquired during the North Atlantic Tracer Release Experiment (NATRE) at 26°N, 29°W (Ferrari and Polzin 2005)

$K_e(z)$ as a function of depth for the TNEA (Fig. 6) by averaging $K_e^{(2)}$ between 4°N and 11°N.

3.4 Diagnosis of oxygen variance production with the extended Osborn–Cox model

The basic approach to analyze tracer variability (be it temperature, salinity or oxygen) is the Reynolds decomposition. For the case of temperature, Osborn and Cox (1972) found a simple relation between the generation and dissipation of tracer variance known as the Osborn–Cox model. However, Ferrari and Polzin (2005) elucidate that mesoscale dynamics are not considered as an individual process within the Reynolds decomposition and the standard Osborn–Cox relation, and applied a triple decomposition⁹ $C = C_m + C_e + C_t$, where C_m , C_e and C_t are defined as the tracer mean,¹⁰ the tracer fluctuations on the mesoscale and the tracer fluctuations on the microscale, respectively. Within their study they derive a parameterized tracer variance budget (extended Osborn–Cox model) for the steady and homogeneous state:

⁹ Even though oxygen is a non-conservative tracer, we will apply it here in the Reynolds decomposition, since the time scales of local oxygen change due to generation or consumption are much larger than the time scales and magnitude of oxygen variability due to physical processes.

¹⁰ As mentioned earlier, in isopycnal coordinates this should be a thickness-weighted average.

$$\underbrace{K_e |\nabla_\sigma C_m|^2}_{[1]} + \underbrace{K_\rho (\nabla_\sigma^\perp C_m)^2}_{[2]} = \underbrace{\frac{1}{2} \kappa_C \langle |\nabla C_t|^2 \rangle}_{[3]} \quad (11)$$

with eddy diffusivity K_e , mean isopycnal tracer gradient $\nabla_\sigma C_m$, diapycnal diffusivity K_ρ , mean diapycnal tracer gradient $\nabla_\sigma^\perp C_m$ and molecular diffusivity κ_C of the tracer C . The operator $\langle \cdot \rangle$ denotes the average on spatial scales that are large compared to mesoscale fluctuations but small compared to the mean field (Ferrari and Polzin 2005). The terms in (11) can be summarized in a schematic, which was originally proposed by Garrett (2001) and further discussed by Ferrari and Polzin (2005). Term [1] represents the generation of tracer variance by the mesoscale, i.e. mesoscale eddies act on a mean isopycnal tracer gradient and generate variability on the fine- to mesoscale [O(0.1–100) km]. Term [2] describes the generation of tracer variance on the microscale, i.e. diapycnal mixing acts on the mean diapycnal tracer gradient and generates variance on the microscale [O(10^{-3} –1) m]. Term [3] represents the dissipation of tracer variance on the molecular scale.

Within this study, we use (11) to estimate the generation of oxygen variance by mesoscale stirring [1] and diapycnal mixing [2] as a function of density and latitude. Even though a proof of the oxygen variance budget is not possible since no appropriate measurements with a fast response oxygen sensor were available to estimate oxygen variance dissipation, we can compare the role of these two generation processes in the TNEA (Fig. 7).

We derive the mean diapycnal oxygen gradient from the mean hydrographic section along 23°W as given in (1), i.e. $C_m \hat{=} \bar{C}$. The mean isopycnal oxygen gradient is calculated according to (6).

The diapycnal diffusivity K_ρ was determined from microstructure measurements by Fischer et al. (2013), who proposed a constant profile over depth between 150 and 500 m for the TNEA with $K_\rho = 1.0 \times 10^{-5} \text{ m}^2 \text{ s}^{-1}$. This value is in general agreement with the value of $(1.19 \pm 0.18) \times 10^{-5} \text{ m}^2 \text{ s}^{-1}$ as obtained from a tracer release experiment carried out at 8°N, 23°W at 350 m depth (Banyte et al. 2012). To estimate the variance production by diapycnal mixing for a density range that is associated with a depth range of 100–1,000 m, we extrapolated K_ρ by assuming a constant diapycnal diffusivity.

The average depth profile of the eddy diffusivity K_e for the TNEA is estimated as shown in Sect. 3.3.

3.5 Oxygen flux, time scales, and oxygen supply

This section is separated into 3 subsections. In (a) both shipboard and moored observations are used to estimate the eddy-driven meridional oxygen flux along 23°W. By

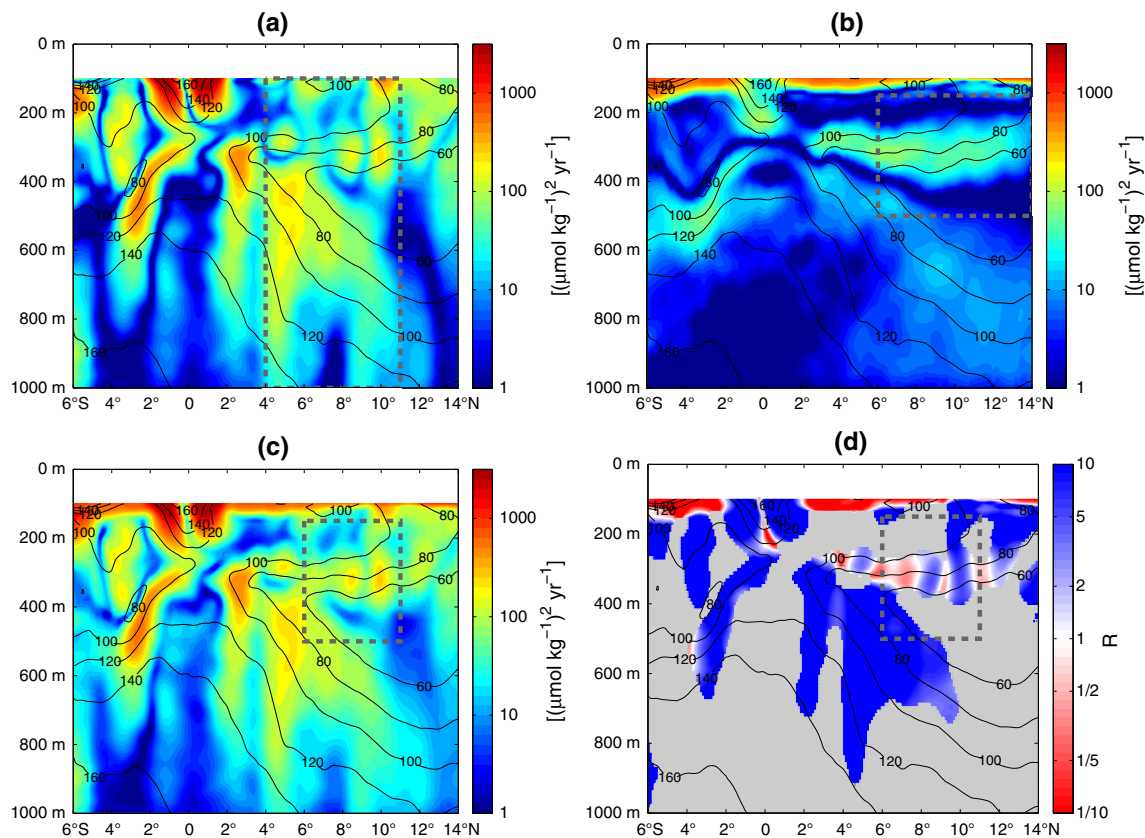


Fig. 7 23°W sections (6°S–14°N) of **a** O₂ variance production by mesoscale stirring, **b** O₂ variance production by diapycnal mixing, **c** total O₂ variance production induced by mesoscale stirring and diapycnal mixing (sum of **a** and **b**) and **d** ratio R of O₂ variance production terms (mesoscale stirring over diapycnal mixing). Gray areas in **d** define regions with a total O₂ variance production of

$<50 (\mu\text{mol kg}^{-1})^2 \text{ year}^{-1}$. In all four panels the mean oxygen distribution is superimposed as black contour lines. Gray dashed boxes in all four panels mark regimes where the analysis was based on a quantitative estimate of the eddy diffusivity K_e as well as the diapycnal diffusivity K_p

applying and comparing two different approaches the reliability of the estimates is tested. In (b) moored observations are used to study time scales of variability of velocity, oxygen and the corresponding oxygen flux. In (c) the eddy-driven meridional oxygen supply is derived and the oxygen budget of the TNEA is introduced.

3.5.1 Eddy-driven meridional oxygen flux

Two different methods are applied in this section to determine the eddy-driven meridional oxygen flux along 23°W: (1) a diffusive flux parameterization (as described in Sect. 3.3) using the estimated mean profile of the eddy diffusivity (Sect. 3.3) and the mean meridional oxygen¹¹ section (Sect. 3.1) to calculate a meridional section of the meridional oxygen flux and (2) a correlation of oxygen and meridional velocity time series acquired from the 5°N,

23°W and 8°N, 23°W moorings to estimate local oxygen fluxes. In order to distinguish between both methods in the following, we define the oxygen flux based on the diffusive flux parameterization as F^d and the oxygen flux based on the mooring time series as F' .

The generally diffusive character of a tracer flux in the meridional direction was shown by Kamenkovich et al. (2009). Greatbatch et al. (2007) considered the diffusive flux parameterization to study the importance of eddy-induced mixing on the meridional heat transport.

We write the diffusive flux parameterization in density coordinates because a fluid particle generally moves along a neutral density surface (McDougall 1987):¹²

$$F^d(\sigma_\theta, \phi) = -K_e(\sigma_\theta) \nabla_{\sigma_\theta} \overline{O_2}(\sigma_\theta, \phi) \quad (12)$$

Here, K_e is the mean eddy diffusivity profile for the TNEA as described in Sect. 3.3. Since K_e is given as a function of

¹¹ Here we assume that oxygen consumption can be neglected on time scales of eddy-driven mixing. For that reason we consider oxygen as a conserved quantity in the tracer conservation equation.

¹² Neutral density surfaces are defined locally, but are not necessarily existing continuously. Here, we base our calculations on surfaces of potential density referred to the ocean surface.

depth, we transform it onto density coordinates by using the mean depth of the density surfaces $\bar{z}(\sigma_\theta, \phi)$ estimated from the mean hydrographic section. $\nabla_{\sigma_y} \bar{O}_2$ is the mean meridional oxygen gradient along an isopycnal surface—the mean oxygen, \bar{O}_2 , is calculated according to (1). A constant thickness of an isopycnal layer with respect to latitude is assumed here (since the depth of the potential density surfaces is rather constant over latitude, cf. Fig. 1) such that a thickness weighting of the mean oxygen distribution \bar{O}_2 was neglected in (12).

The second method to determine the meridional oxygen flux is given by the correlation of meridional velocity and oxygen time series. We estimate the turbulent meridional oxygen flux¹³ with

$$F'(z_I) = \overline{v'O'_2} \quad (13)$$

where v' and O'_2 are the velocity and oxygen time series anomalies with respect to density surfaces. $F'(z_I)$ can be interpreted as the flux at the instrument depth z_I being a weighted average over all isopycnal surfaces that were sampled by the instrument during the mooring period. A detailed description of the derivation of (13) as well as its error estimate is given in Appendix 2.

In general, (13) contains a divergent flux and a rotational flux component. The rotational flux component does however not contribute to the mean tracer budget at all. From a single mooring location it is impossible to estimate the divergent component of the tracer flux that contributes to the mean tracer budget. Nevertheless, Marshall and Shutts (1981) and Eden et al. (2007) show that rotational tracer fluxes are coupled to the strength of the divergence of the advective flux of tracer variance, which, in turn, is related to the mean current field and thus provides a justification for the assumption that rotational tracer fluxes are rather small in regions with a weak mean flow.

Within this study we use time series of meridional velocity and oxygen from 5°N, 23°W and 8°N, 23°W, which were recorded simultaneously during the mooring periods November 2009–October 2012 and May 2011–October 2012, respectively (see Tables 2, 3 for details) to estimate the local meridional oxygen flux with (13). At the mooring positions weak mean currents are present at depth (cf. Fig. 4a) and we thus assume a weak contribution of rotational tracer fluxes to our flux estimates in (13). We expect the largest bias due to rotational tracer fluxes at shallow depths (100 and 200 m) since a stronger mean flow due to the NECC/NEUC and the nNECC current band at 5°N and 8°N, respectively, exists.

¹³ The total meridional oxygen flux is Reynolds decomposed as $F = \bar{F} + F'$. Here, only the turbulent meridional oxygen flux F' is investigated (see Appendix 2 for details).

Since we are interested in the eddy-driven meridional oxygen flux, we excluded the velocity and oxygen variability on time scales of the inertial period and shorter by low-pass filtering¹⁴ the time series anomalies v' and O'_2 with a cutoff frequency corresponding to a period of 10 days (inertial period is $T_i = 5.7$ days and $T_i = 3.6$ days at 5°N and 8°N, respectively). Indeed, a time-scale analysis of the contributing fluctuations [cf. the following Sects. 3.5.2, 4.5.2] shows that short-term fluctuations have no effect on the magnitude but merely on the uncertainty of the estimated oxygen flux (cf. Fig. 11c, d).

3.5.2 Time scales of velocity, oxygen and meridional oxygen flux

The high temporal resolution of the oxygen and velocity time series from the 5°N, 23°W and 8°N, 23°W moorings allows a Fourier analysis of these data sets. In order to identify the dominant time scales that contribute to the oxygen flux in (13), we additionally applied a low-pass filter¹⁵ $L(\tau)$ with different cutoff periods τ on the time series anomalies, i.e.

$$L_\tau v' = L(\tau) \times v'; \quad L_\tau O'_2 = L(\tau) \times O'_2 \quad (14)$$

and we calculated the oxygen flux as a function of the filter period τ :

$$L_\tau F'(z_I) = \overline{L_\tau v' L_\tau O'_2} \quad (15)$$

$L_\tau F'(z_I)$ can be interpreted as the cumulative oxygen flux resulting from processes on time scales between the filter period τ and the total length of the time series T_{max} . The error of $L_\tau F'(z_I)$ was calculated as the standard error for an arithmetic mean [see (28) in Appendix 2].

3.5.3 Eddy-driven meridional oxygen supply and the oxygen budget in the TNEA

Based on the diffusive flux parameterization (12) the eddy-driven meridional supply of oxygen was estimated. Meridional loss or gain of oxygen due to eddy fluxes is given by the meridional divergence of the oxygen flux on an isopycnal surface, which is the meridional derivative $-\nabla_{\sigma_y} F^d$. Using the diffusive flux parameterization (12) the meridional oxygen supply along 23°W is then given by

¹⁴ Here, a butterworth filter of 3rd order was used.

¹⁵ Here, a running mean was applied with a rectangular filter window, where the window length was defined as the cutoff period. The reason for using a running mean instead of a butterworth filter is that a zero oxygen flux for large filter periods could be ensured (due to weak edge effects of the filter), which has to be given by definition (since time series anomalies were used for the correlation).

$$-\nabla_{\sigma} F^d(\sigma_{\theta}, \phi) = K_e(\sigma_{\theta}) \nabla_{\sigma}^2 \overline{O_2}(\sigma_{\theta}, \phi) \quad (16)$$

In writing (16), we assumed K_e to be independent on latitude. We considered this a valid approach, since meridional variations in K_e were small compared to its uncertainty (cf. Sect. 3.3).

Fischer et al. (2013) gave a first estimate of the oxygen budget for the TNEA. They derived a mean profile of the diapycnal oxygen supply for the upper half of the TNEA OMZ (120–570 m) in the box 6°N–15°N and 30°W–15°W. Based on the oxygen consumption profile for the TNEA (Karstensen et al. 2008) and the assumption of a steady state, they proposed a residual oxygen supply reflecting the zonal and meridional isopycnal ventilation of the OMZ.

Here, we combined our results regarding the eddy-driven meridional oxygen supply with the results of Karstensen et al. (2008) and Fischer et al. (2013) to further refine the picture of the ventilation of the TNEA OMZ. Following Fischer et al. (2013) we analyzed (16) in a similar latitudinal range (6°N–14°N) and calculated an average vertical profile of the eddy-driven meridional oxygen supply for this regime. The error of this profile was estimated as follows. For every individual research cruise with a representative CTD/ O_2 section along 23°W (cf. Table 1) a 2nd order polynomial fit was applied to the oxygen data for every single potential density surface to estimate the curvature of the meridional oxygen distribution between 6°N and 14°N. Double the standard deviation σ of all oxygen curvatures was used to estimate the standard error $\Delta = 2\sigma/\sqrt{N}$ [with N the number of all (independent) research cruises] for the average oxygen curvature on a 95 % confidence level. Multiplication of Δ with the eddy diffusivity yielded the error of the mean meridional oxygen supply due to the uncertainty of the oxygen curvature which was estimated to about $2.8 \mu\text{mol kg}^{-1} \text{ year}^{-1}$ at 120 m, decreased to $0.6 \mu\text{mol kg}^{-1} \text{ year}^{-1}$ at 300 m and yielded $0.3 \mu\text{mol kg}^{-1} \text{ year}^{-1}$ at depth of the OMZ (350–570 m). Combined with the assumed uncertainty of the eddy diffusivity K_e (factor of 2, see Sect. 3.3), the total error of the mean meridional oxygen supply in (16) was estimated using the standard formula for the error propagation. At depth of the OMZ, we found a strong/weak error due to the uncertainty of the eddy diffusivity/oxygen curvature.

The steady state assumption for the oxygen budget in the TNEA (Fischer et al. 2013) is in general invalid, as Stramma et al. (2008b) determined a significant average oxygen decrease in the TNEA OMZ ($-0.34 \pm 0.13 \mu\text{mol kg}^{-1} \text{ year}^{-1}$) over the last decades. Thus, we included in the oxygen budget the oxygen trend observed for the last decades (about 25 years). This trend (oxygen tendency) must balance the sum of all other terms (consumption and supply) that contribute to the oxygen budget.

Using above considerations the oxygen budget can be written as

$$aOUR + O_{2,dia} + O_{2,y,eddy} + R_{O_2} = \partial_t O_2 \quad (17)$$

where $aOUR$ is the apparent oxygen utilization (AOU) rate (oxygen consumption), $O_{2,dia}$ represents the diapycnal oxygen supply, $O_{2,y,eddy}$ is the eddy-driven meridional oxygen supply, R_{O_2} defines the residual oxygen supply due to mean advection and zonal eddy diffusion and $\partial_t O_2$ defines the oxygen tendency of the TNEA OMZ.

In order to estimate a mean depth profile for the oxygen tendency $\partial_t O_2$ in the TNEA OMZ, we used the AOU of the two periods 1999–2008 and 1972–1985, that was estimated on neutral surfaces by Brandt et al. (2010) along 23°W. We calculated the mean AOU profile for each of the two time periods as an average (6°N–14°N) over the anomalies¹⁶ of all given CTD/ O_2 profiles and eventually took the difference of both mean AOU profiles to get the mean oxygen tendency. **AOU instead of oxygen was used in order to account for a possible temperature effect on the oxygen saturation concentration of sea water, since the oxygen tendency over several decades is discussed.**¹⁷ The uncertainties of the AOU for both periods were estimated as double the standard error from the anomalies of all individual CTD/ O_2 profiles obtained for the considered latitude range within the two periods. Finally, the error for the oxygen tendency (95 % confidence) was estimated based on the AOU errors from both periods using the standard formula for the error propagation, that is $\Delta \partial_t O_2 = \sqrt{(\Delta AOU_1)^2 + (\Delta AOU_2)^2}$.

4 Results

4.1 Mean oxygen and oxygen variability

Based on repeat shipboard CTD/ O_2 sections we estimated the mean oxygen and the oxygen variability in the TNEA along 23°W (Fig. 1). Strong oxygen variability was observed at the upper and southern boundary of the OMZ, in the equatorial regime as well as at shallow depths above 200 m over a wide latitudinal range between 4°N and 14°N.

In order to obtain an estimate of the uncertainty of the oxygen variance section from shipboard observations (Fig. 1b) we compared it with the mooring based oxygen variance profiles for the four mooring positions (Fig. 3).

¹⁶ Referred to the mean field along the 23°W section.

¹⁷ Indeed, this effect is very small and does not change the oxygen tendency significantly.

We found a good correspondence between profiles derived from shipboard and moored observations for all four latitudes suggesting that the oxygen variance section can indeed be regarded as a reasonable estimate of the oxygen variability in the Tropical Atlantic along 23°W.

4.2 Characteristic eddy velocity and mean zonal velocity along 23°W

We used the velocity time series from the 5°N, 23°W mooring position to parameterize [(19) and (20) in Appendix 1] the effect of the velocity variability on time scales lower than 10 days (e.g. inertial and tidal oscillations) on the total velocity variability (Fig. 5a). The variability of the filtered velocities σ_{Lu} and σ_{Lv} (standard deviation of low-pass filtered velocity) is clearly smaller than the variability of the unfiltered velocities σ_u and σ_v . Since the parameterization works well for moderate magnitudes of velocity variability, we applied it to the 23°W velocity section from shipboard observations. For 5°N, the variability from the unfiltered and the filtered velocities (calculated both from shipboard and mooring data) using $\sqrt{(\sigma_u^2 + \sigma_v^2)/2}$ and $U_e = \sqrt{(\sigma_{Lu}^2 + \sigma_{Lv}^2)/2}$, respectively, are shown as a depth profile in Fig. 5b. Whereas the variability of the unfiltered velocities yields about 10–11 cm s⁻¹ at 100 m and drops down to 5 cm s⁻¹ at 700 m, the characteristic eddy velocity U_e is smaller by about 2 cm s⁻¹ for almost the whole depth range. The U_e profiles from both data sets match well, hence in the following we used the corrected 23°W velocity section based on shipboard observations to estimate U_e in the whole domain.

The mean zonal velocity as well as the characteristic eddy velocity U_e along 23°W calculated from repeat ship sections are shown in Fig. 4a, b, respectively. For the equatorial Atlantic, Brandt and Eden (2005), Brandt et al. (2006), Bunge et al. (2008) and Brandt et al. (2012) show that a high percentage of the velocity fluctuations results from intraseasonal variability (e.g. TIWs) as well as from the seasonal cycle of the zonal currents and from variability on interannual time scales leading to an overestimation of U_e , which might explain the strong equatorial maximum in Fig. 4b between 6°S and 4°N. Enhanced variability was also found between 11°N and 14°N, but it remains unclear whether this is the result of mesoscale or annual to longer-term fluctuations. Hence, for our further analysis we considered the estimated U_e in the region between 4°N and 11°N.

Figure 4c shows the ratio of absolute mean zonal velocity over characteristic eddy velocity. Even though U_e was overestimated between 6°S and 4°N, it is evident that the equatorial region is dominated by mean zonal

advection, whereas the region from 5°N to 11°N is characterized by a comparatively strong mesoscale activity.

4.3 Eddy diffusivity for the Tropical North East Atlantic Ocean

We conducted the four steps as described in Sect. 3.3 to estimate a mean eddy diffusivity profile $K_e(z)$ for the TNEA as an average between 4°N and 11°N (Fig. 6). It reaches values of about 1,350 m² s⁻¹ at 100 m and decays to values below 300 m² s⁻¹ at 800–1,000 m depth, which is in principle a function of the characteristic eddy velocity U_e (cf. Fig. 5b). For comparison we show the meridional eddy diffusivity at 300 m depth estimated from the Guinea Upwelling Tracer Release Experiment (carried out at 8°N, 23°W) in a study by Banyte et al. (2013). They estimated a meridional eddy diffusivity of 500 m² s⁻¹ (± 200 m² s⁻¹) for the TNEA at 300 m depth. Both estimates are in good agreement with each other. Additionally, the eddy diffusivity profile estimated from data acquired in the framework of the North Atlantic Tracer Release Experiment (NATRE) at about 26°N, 29°W (Ferrari and Polzin 2005) is included. It is larger at depths from 200 to 700 m and drops down to a similar magnitude at depths from 800 to 1,000 m.

In the following we applied the obtained $K_e(z)$ profile to estimate the oxygen variance production due to mesoscale stirring (Sect. 4.4) as well as the eddy-driven meridional oxygen fluxes and supply along the 23°W section (Sect. 4.5). For this analysis we considered the region from 6°S to 14°N to show also qualitative differences between the equatorial region and the OMZ regime. Strictly speaking these estimates are valid only in the latitude range from 4°N to 11°N.

4.4 Oxygen variance production

We calculated the oxygen variance production due to mesoscale stirring (Fig. 7a) and diapycnal mixing (Fig. 7b) as defined in the extended Osborn–Cox relation [left hand side of (11)]. Both terms describe how much oxygen variance ($\mu\text{mol kg}^{-1}$)² is generated within the time period of 1 year.

The sum of both terms reflects the total oxygen variance production and is shown in Fig. 7c. Evidently, high oxygen variance production occurs at the southern boundary (5°N–8°N, 400–700 m) and the upper boundary (5°N–12°N, 300 m) of the OMZ, whereas the interior of the OMZ shows little oxygen variance production.

In order to evaluate the contribution of either process to the total oxygen variance production, we calculated the ratio of both terms, i.e.

$$R = \frac{K_e |\nabla_\sigma O_{2m}|^2}{K_\rho (\nabla_\sigma^\perp O_{2m})^2} \quad (18)$$

The result is shown in Fig. 7d. For $R \gg 1$ mesoscale stirring along isopycnal surfaces is the main producer of the oxygen variance, whereas for $R \ll 1$ diapycnal mixing is the larger variance production term. $R \sim 1$ indicates that both processes contribute to the variance production in the same order of magnitude. We found that the local oxygen variance maximum at the southern boundary of the OMZ (Fig. 1b, 5°N–8°N, 400–700 m) is dominantly produced by mesoscale stirring. The local oxygen variance maximum at the upper boundary of the OMZ (Fig. 1b, 5°N–12°N, 300 m) is generated by both mesoscale stirring and diapycnal mixing.

4.5 Meridional oxygen flux, time scales and meridional oxygen supply

4.5.1 Eddy-driven meridional oxygen flux

Based on shipboard observations the eddy-driven meridional oxygen flux along the 23°W section was calculated on potential density surfaces using the flux gradient parameterization (12) and was projected back onto depth coordinates afterward (Fig. 8). Reddish/bluish colors define a northward/southward eddy-driven oxygen flux, respectively. Black contour lines represent oxygen isolines in interval steps of $20 \mu\text{mol kg}^{-1}$. Between the southern boundary and the interior of the OMZ (in a depth range 400–700 m), we find a northward oxygen flux, which continuously decreases from 5°N toward north, drops to zero at the core of the OMZ (11°N) and turns into a southward flux north of 11°N. Between 100 and 400 m, meridionally alternating bands of north- and southward oxygen flux are dominant. Near the equator, we mainly find poleward directed oxygen fluxes.

Based on the 5°N, 23°W and 8°N, 23°W mooring data, we calculated the eddy-driven meridional oxygen flux via correlation using (13).¹⁸ Figure 9a, b show the comparison of both flux approaches [parameterization, (12), and correlation, (13)] at 5°N, 23°W and 8°N, 23°W, respectively. For 5°N, 23°W, both estimates match well within the error at depths from 100 to 500 m. Nevertheless, at 100 and 200 m the stronger meridional oxygen flux calculated from the mooring data as well as its estimated error reflect a high variability of oxygen flux at these depths, which gets

¹⁸ The time series anomalies were low-pass filtered to remove inertial and tidal variability before applying (13). However, as shown in Sect. 4.5.2 and corresponding Fig. 11c, d, short term fluctuations do not contribute to the turbulent meridional oxygen flux but rather to its uncertainty.

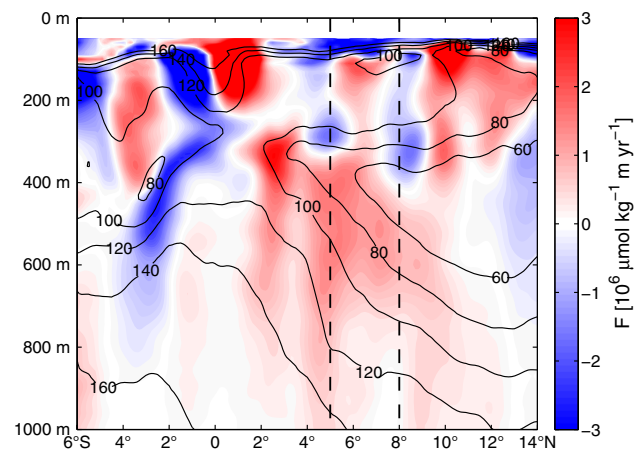


Fig. 8 Eddy-driven meridional oxygen flux along 23°W calculated using the diffusive flux parameterization (12). Positive/negative values mark an eddy-driven oxygen flux directed towards north/south. Superimposed black contour lines mark the mean oxygen distribution. Dashed vertical lines mark mooring positions 5°N and 8°N that are considered in Fig. 9a, b. Note that the analysis was based on a quantitative estimate of the eddy diffusivity profile $K_e(z)$ being an average of the regime 4°N–11°N

smaller at depths from 300 to 500 m. At depths from 600 to 800 m the correlation method generally shows a smaller and southward directed oxygen flux, whereas the parameterized flux is stronger and directed to the north. For 8°N, 23°W (Fig. 9b) both flux estimates agree well within the error at almost all depths between 100 and 800 m. Similar to 5°N, 23°W a high variability of the oxygen flux is found at 100 and 200 m depth. The southward oxygen flux between 100 and 300 m, which turns into a northward oxygen flux at depths from 400 to 800 m is well represented by both estimates.

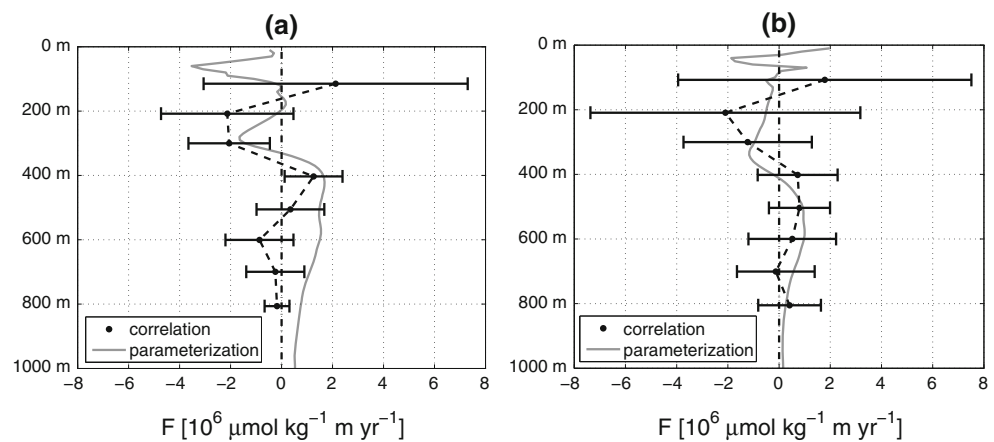
4.5.2 Time scales of velocity, oxygen and meridional oxygen flux

Time scales of velocity and oxygen variations responsible for the meridional oxygen flux were analyzed from the 5°N, 23°W and 8°N, 23°W mooring data and are presented throughout this section.

Figure 10a, b show the low-pass filtered (cutoff frequency corresponding to a period of 10 days) oxygen and meridional velocity time series from 5°N, 23°W at 400 and 500 m depth (core depth of OMZ), respectively. The corresponding turbulent meridional oxygen flux, that was calculated via correlation using (13), is 1.3×10^6 and $0.3 \cdot 10^6 \mu\text{mol kg}^{-1} \text{ m year}^{-1}$ at 400 and 500 m depth, respectively (cf. Fig. 9a).

The time series of oxygen and meridional velocity in Fig. 10a, b reveal fluctuations on intraseasonal to seasonal time scales (short term fluctuations are not present due to the applied low-pass filter) that contribute to the observed

Fig. 9 **a** Eddy-driven meridional oxygen flux at 5°N, 23°W calculated via correlation of mooring time series (black dots with error bars) and via diffusive flux parameterization (gray line) as it is shown in Fig. 8. For the correlation the meridional velocity and oxygen time series were low-pass filtered with a cutoff frequency corresponding to a period of 10 days. **b** Same as **a**, but at 8°N, 23°W



meridional oxygen flux. A detailed discussion using frequency analysis is given throughout the following paragraphs.

However, we first want to focus on seasonal variations in oxygen that are likely caused by the seasonal variability of the eastward directed NEUC at 5°N and in turn are likely responsible for seasonal variations in the turbulent meridional oxygen flux. Indeed, an analysis of the annual harmonic of zonal velocity indicates an amplitude of 1 cm s^{-1} (not shown) at depths of 400 and 500 m. About 2 months after maximum eastward velocity, the annual harmonic of oxygen is at maximum (not shown) suggesting a seasonal variation in the zonal ventilation at the southern rim of the OMZ. In order to study this effect on the turbulent meridional oxygen flux, we fitted an annual harmonic to the time series of the product of oxygen and meridional velocity anomalies ($v'O_2'$) as given from the time series in Fig. 10a, b, respectively. The results represent the annual harmonic of the turbulent meridional oxygen flux and are shown for 400 and 500 m depth by the solid lines in Fig. 10c, d, respectively. The mean turbulent meridional oxygen flux [as given by (13)] is marked by the thick dashed lines. Positive and negative phases of the annual cycle of the turbulent meridional oxygen flux are marked by gray and white bars. The amplitude of the annual cycle is of comparable magnitude to its mean resulting in phases of enhanced and reduced northward oxygen flux at 400 m or enhanced northward and reversed (southward) oxygen flux at 500 m.

The power spectral density (PSD) of the unfiltered meridional velocity and oxygen, respectively, is shown for depths of 400 and 500 m for 5°N in Fig. 11a, b and for 8°N in Fig. 12a, b (comparable characteristics were obtained for other depths between 100 and 800 m). In the double logarithmic presentation, idealized spectral slopes associated with turbulence theory (see Sect. 5 for a qualitative discussion) are shown for both velocity and oxygen spectra as gray dashed and dash-dotted lines, respectively.

At 5°N (Fig. 11a, b) the meridional velocity shows a band of high energy for periods of 30–60 days, which corresponds to the period of TIWs. Time scales of TIWs have been reported e.g. by Athie and Marin (2008), who determined a dominant variability in the period band between 25 and 50 days. A second maximum was found close to the inertial period ($T_i = 5.7$ days) with enhanced energy between 3 and 6 days corresponding to near-inertial oscillations of the ocean. Semidiurnal and diurnal tidal oscillations could be observed as well. Between the inertial period T_i and the period range of TIWs, we found a distinct minimum of wave energy. In contrast, the oxygen PSD shows a more linear decrease in the double logarithmic presentation from low frequencies to high frequencies with only weak maxima in the period range of TIWs and near-inertial oscillations. Comparing the spectral slopes between 10 and 30 days the velocity spectra exhibit a stronger roll off than the oxygen spectra.

At 8°N (Fig. 12a, b) the meridional velocity shows high energy for periods larger than 35 days. The second energy maximum, corresponding to near-inertial oscillations, was also found, but it is shifted to lower periods (2–4 days) due to the lower inertial period at 8°N ($T_i = 3.6$ days). Hence, a broader minimum of wave energy between the inertial period and the period range of the mesoscale was observed. Similar to 5°N, the oxygen PSD shows a more linear decrease in double logarithmic presentation from low to high frequencies, but the maxima at the inertial period and the period range of the mesoscale as well as the minimum in between are slightly more pronounced at least at 500 m (also at depths of 600–800 m, not shown). Again, the velocity spectrum exhibits a stronger roll off than the oxygen spectrum between 10 and 30 days.

Figure 11c, d show the turbulent meridional oxygen flux at 5°N at 400 and 500 m, respectively, as a function of the low-pass filter period τ (black circles). It is defined as the cumulative oxygen flux $L_\tau F'$ [cf. (15)] on time scales between τ and the time length T_{max} ($=1,094$ days) of the

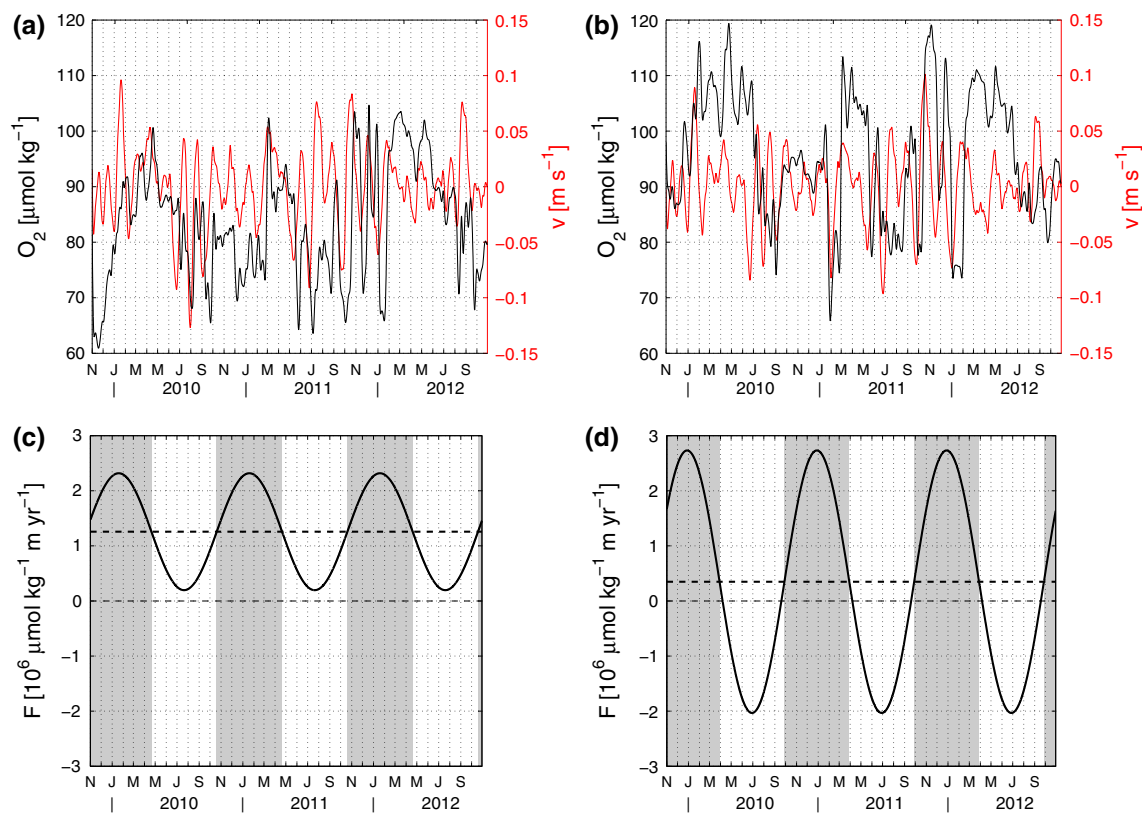


Fig. 10 Time series of oxygen (black) and meridional velocity (red) from 5°N , 23°W at **a** 400 m and **b** 500 m depth. The time series were low-pass filtered with a cutoff frequency corresponding to a period of 10 days. Lower panels (**c** 400 m and **d** 500 m depth) show the mean turbulent meridional oxygen flux (thick dashed line) estimated from

the correlation of oxygen and meridional velocity (as given in **a** and **b**). Additionally, the annual harmonic of the turbulent meridional oxygen flux (solid line) is shown. Gray and white bars mark the positive and negative phases of the estimated annual cycle

mooring time series.¹⁹ For the limit $\tau \rightarrow 0$, the cumulative oxygen flux includes processes on all time scales smaller than the total time period of the time series down to double the sampling interval of 2 h. Strong changes in the cumulative oxygen flux within a certain period band are associated with a strong oxygen flux in this band. Here, we found strong oxygen fluxes for the period band from 10 to 80 days, which corresponds to the period range of meso-scale variability. By taking into account the annual harmonic analysis (shown in Fig. 10c, d), the annual variability of the cumulative oxygen flux was estimated (Fig. 11c, d). The dark/light gray circles represent the cumulative oxygen flux during the positive/negative phase of the annual cycle that are illustrated by the gray and white regimes in Fig. 10c, d. During the positive half period the cumulative oxygen flux is much stronger towards the north, whereas during the negative half period the flux is almost zero (at 400 m) or even directed to the south (at 500 m).

¹⁹ By definition, the cumulative oxygen flux is zero for $\tau \rightarrow T_{\max}$, since the calculation is based on the time series anomalies.

Similarly, the cumulative oxygen flux as a function of the low-pass filter period τ was calculated for 8°N at 400 and 500 m depth (Fig. 12c, d). At 400 m most of the oxygen flux was observed in two period bands. In the period band between 80 and 300 days a northward oxygen flux was observed, whereas at periods between 10 and 80 days the flux was weaker and directed to the south. Summing up the flux on all time scales (i.e. $\tau \rightarrow 0$) yielded a northward oxygen flux. At 500 m depth, a northward oxygen flux was observed, mainly driven on time scales between 10 and 100 days. An annual variability of the oxygen flux could not be identified due to a too short time series (time length of the analyzed time series was 533 days).

4.5.3 Eddy-driven meridional oxygen supply and the oxygen budget in the TNEA

Figure 13 shows the eddy-driven meridional oxygen supply along 23°W , which was calculated on potential density surfaces using (16) and consecutively projected onto depth coordinates. Regions with reddish/bluish colors define an

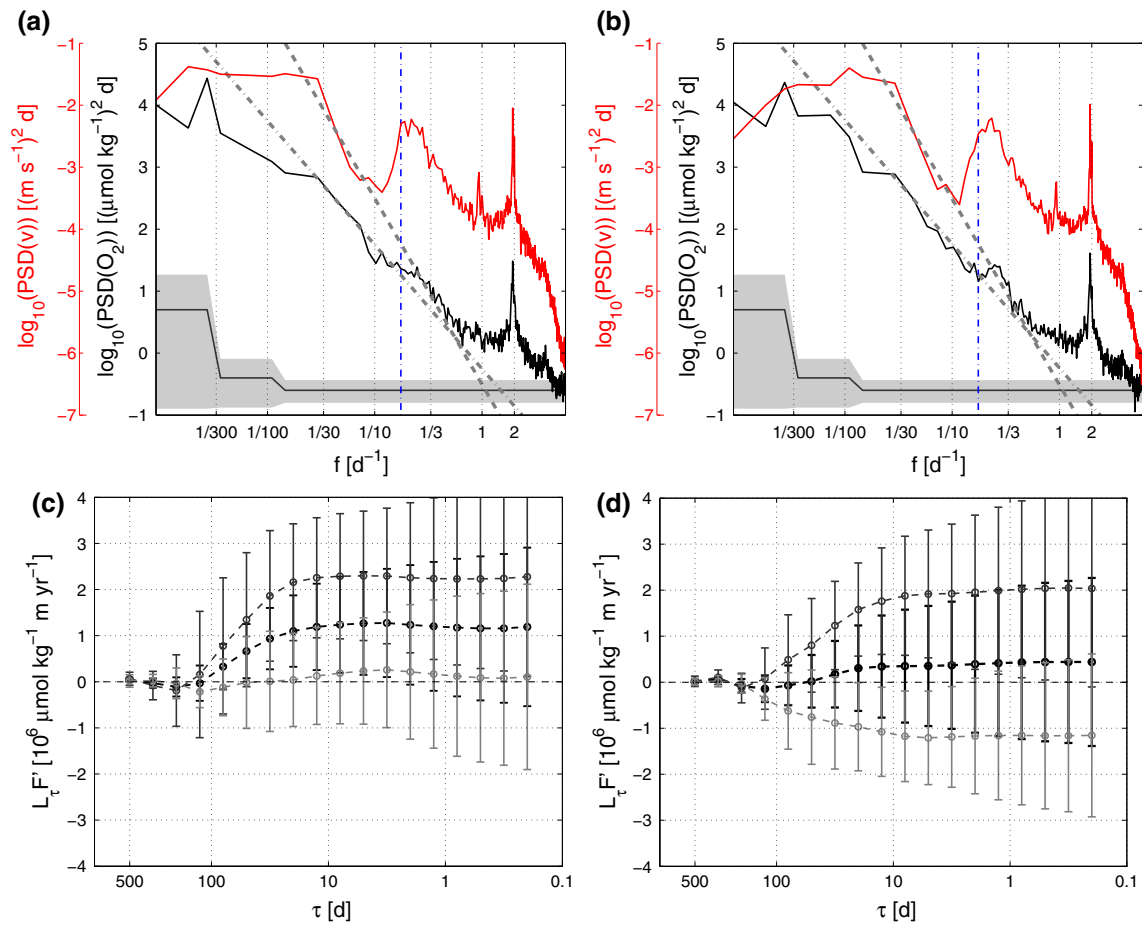


Fig. 11 **a** Power spectral density of meridional velocity (red solid line) and oxygen (black solid line) at 5°N, 23°W at 400 m depth. The 95 % confidence intervals (given by gray shaded area with reference to dark gray solid line in double logarithmic presentation) were calculated by assuming a χ^2 -distribution of the power spectral density. Gray dashed and dash-dotted lines mark spectral slopes associated with f^{-3} and f^{-2} , respectively (for a qualitative discussion of these slopes see Sect. 5). Blue dash-dotted line marks the inertial period $T_i = 5.7$ days for 5°N. **b** Same as **a**, but at 500 m depth. **c** Cumulative turbulent meridional oxygen flux $L_t F^t$ (black circles with black dashed thick line) at 5°N, 23°W at 400 m depth calculated

using (15). The cumulative oxygen flux defines the flux on time scales between the filter period τ and the time length of the mooring time series (here 1,094 days). Error bars were calculated as the standard error of the arithmetic mean. The dark and light gray circles with thin dashed lines represent the cumulative oxygen flux calculated for the positive and negative half period of the annual cycle of the oxygen flux (indicated by the gray and white regimes in Fig. 10c). Both estimates reflect the annual variability of the turbulent meridional oxygen flux. **d** Same as **c**, but at 500 m depth. The corresponding annual cycle of the oxygen flux is shown in Fig. 10d

overall gain/loss of oxygen due to meridional eddy diffusion. At depths between 450 and 600 m, the eddy-driven meridional oxygen supply into the OMZ (gain of oxygen) is rather constant over latitudes between 6°N and 14°N (region marked by the gray dashed box) with an average value of $2.1 \mu\text{mol kg}^{-1} \text{ year}^{-1}$. Above 400 m, latitudinally alternating bands of oxygen loss and gain were observed reaching absolute values of more than $10 \mu\text{mol kg}^{-1} \text{ year}^{-1}$. The equator shows an overall loss of oxygen in the upper 400 m. Above 200 m, oxygen is transported poleward to 2°N and 2°S, where a gain of oxygen was observed. This corresponds to the eddy-driven transport of oxygen out of the EUC core into the lower oxygenated westward current branches north and south of the EUC.

Below 400 m, a maximum oxygen loss was found at about 2°N and 2°S corresponding to the mean positions of the NICC and SICC, which advect oxygen-rich water from the west.

We calculated an average vertical profile of the eddy-driven meridional oxygen supply in the latitudinal range 6°N–14°N (illustrated by the black dashed box in Fig. 13) to refine the given picture of the oxygen budget in the TNEA OMZ regime (cf. Sect. 3.5.3) in the following.

Figure 14 shows the five different terms in (17) contributing to the oxygen budget of the TNEA OMZ regime: consumption, diapycnal supply, eddy-driven meridional supply, residual supply, and tendency. The individual budget terms are explained in the following.

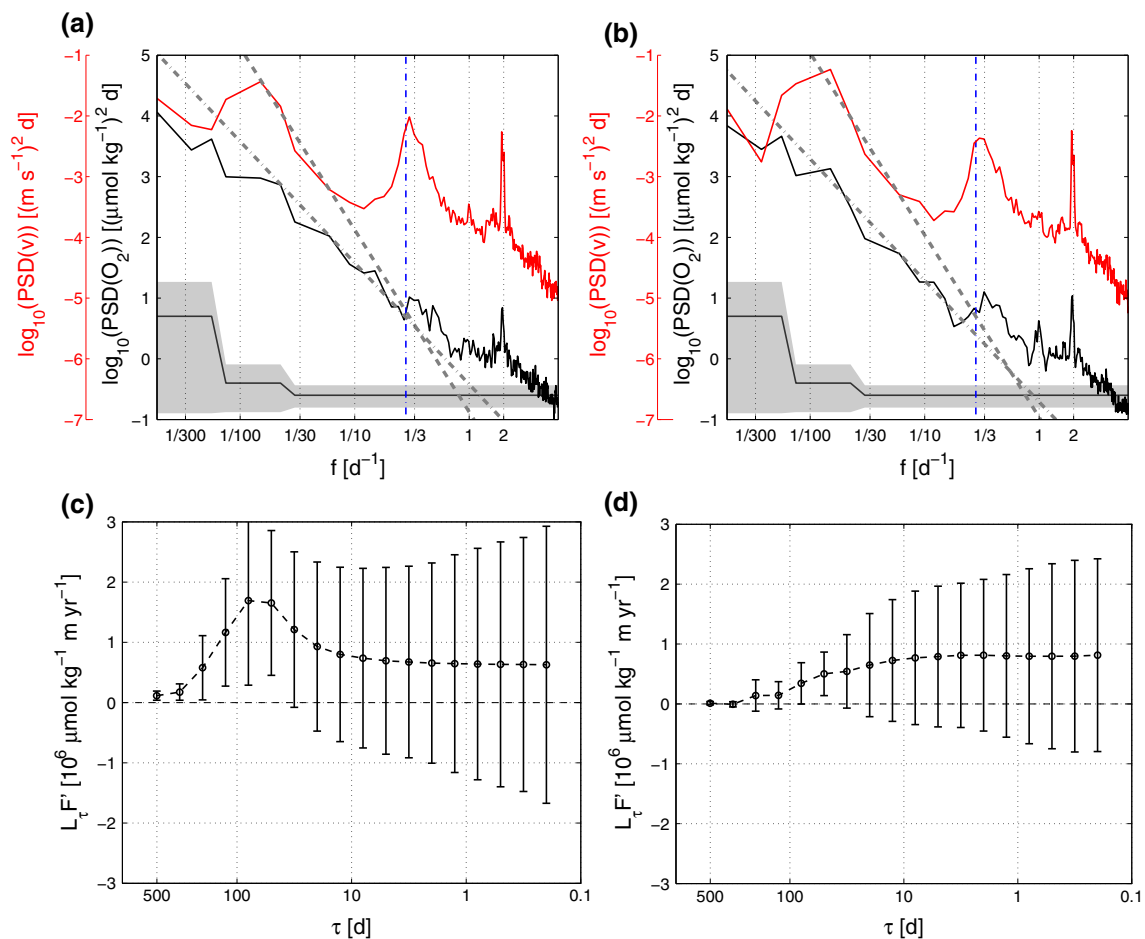


Fig. 12 Same as Fig. 11, but for 8°N , 23°W . The length of the mooring time series was 533 days. The inertial period for 8°N is $T_i = 3.6$ days. In **c** and **d** the annual variability of the turbulent meridional oxygen flux is not included, since the time series was too short for this estimate

Karstensen et al. (2008) proposed an oxygen consumption profile for the Tropical Atlantic with an exponential decay as a function of depth, which is $aOUR(z) = -0.5 + 12e^{-0.0021 \times z}$, with z being depth in m. A 40 % error (95 % confidence) for the oxygen consumption was estimated by the authors. Fischer et al. (2013) estimated the diapycnal oxygen supply with an average error of $0.85 \mu\text{mol kg}^{-1} \text{ year}^{-1}$ (95 % confidence). They showed that diapycnal mixing supplies the OMZ with about $0.9 \mu\text{mol kg}^{-1} \text{ year}^{-1}$ in the depth range 350–570 m with a maximum supply of about $1.7 \mu\text{mol kg}^{-1} \text{ year}^{-1}$ at about 390 m depth. The diapycnal oxygen supply decreases to zero at the upper boundary of the OMZ (deep oxycline). Above, diapycnal mixing contributes to a net oxygen loss in the oxygen-rich Central Waters supplying the OMZ below.

Our estimated mean profile of the eddy-driven meridional oxygen supply shows that mesoscale eddies strongly contribute to the ventilation of the OMZ via meridional pathways, which is $2.4 \mu\text{mol kg}^{-1} \text{ year}^{-1}$ in the depth

range 350–570 m.²⁰ Above this depth range the eddy-driven meridional oxygen supply decreases and in the shallow Central Water layer between 100 and 300 m it is reversed leading to an oxygen loss.

The oxygen tendency profile [cf. Brandt et al. (2010), Sect. 3.5.3] shows a maximum oxygen decrease at a depth of about 340 m, which is slightly below the upper boundary of the OMZ (deep oxycline) and yields $-0.76 \mu\text{mol kg}^{-1} \text{ year}^{-1}$. In the depth range 350 m – 570 m the average oxygen tendency is $-0.43 \mu\text{mol kg}^{-1} \text{ year}^{-1}$.

Based on the estimates of all other budget terms in (17), the residual oxygen supply is rather weak at the depth of the OMZ (on average $0.4 \mu\text{mol kg}^{-1} \text{ year}^{-1}$ in the depth range 350–570 m)²¹ suggesting that most of the

²⁰ The margin of error for this depth range was estimated to $[1.2, 4.8] \mu\text{mol kg}^{-1} \text{ year}^{-1}$ as described in Sect. 3.5.3.

²¹ The average oxygen consumption yields $-4.1 \mu\text{mol kg}^{-1} \text{ year}^{-1}$ between 350 and 570 m.

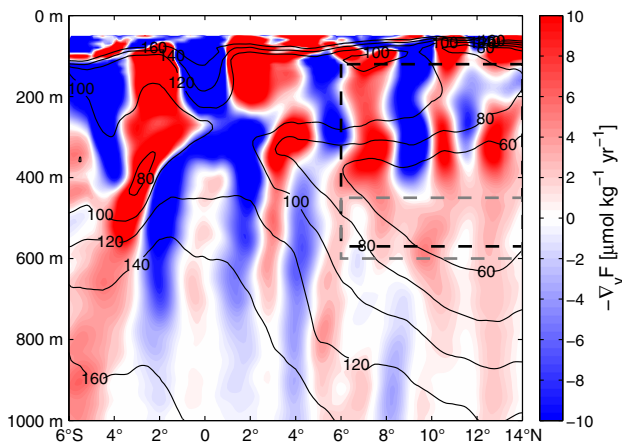


Fig. 13 Eddy-driven meridional oxygen supply along 23°W. *Red-dish/bluish colors* mark gain/loss of oxygen due to meridional oxygen flux. Superimposed *black contour lines* mark the mean oxygen distribution. *Gray dashed box* marks the regime (450–600 m, 6°N–14°N) of a rather homogeneous oxygen supply in the OMZ with an average value of $2.1 \mu\text{mol kg}^{-1} \text{ year}^{-1}$. *Black dashed box* marks the region (120–570 m, 6°N–14°N), for which a mean eddy-driven meridional oxygen supply as a function of depth was calculated and used for the estimate of the oxygen budget in Fig. 14. Note that the analysis was based on a quantitative estimate of the eddy diffusivity profile $K_e(z)$ being an average of the regime 4°N–11°N

ventilation is explained by diapycnal mixing and meridional eddy diffusion. Above 350 m, the residual suddenly increases showing a maximum residual oxygen supply of about $10 \mu\text{mol kg}^{-1} \text{ year}^{-1}$ at 200 m depth.

5 Discussion

The TNEA Ocean is a region of rich oxygen variability with different local oxygen variance maxima spread over the whole 23°W section between 6°S and 14°N at depths of 100–800 m.

Based on the physical processes that lead to oxygen variability, we divide the oxygen variance section into two regimes. The first regime is defined as the well-ventilated equatorial Atlantic (6°S–4°N) with its strong mean and variable zonal currents. The second regime covers the region from 4°N to 14°N. In the upper 400 m, it is characterized by latitudinally alternating zonal currents consisting of two mean eastward current branches, the surface NECC and the subsurface NEUC at 5°N as well as the nNECC at 9°N, meridionally surrounded by westward flow (Garzoli and Katz 1983; Garzoli and Richardson 1989; Urbano et al. 2006). The currents are strong in the upper 200 m and become much weaker below. Below 400 m, a sluggish flow regime with weak mean zonal currents exists, where mesoscale eddy fluxes and small scale diapycnal fluxes play a major role in the ventilation [cf. Fig. 4; a

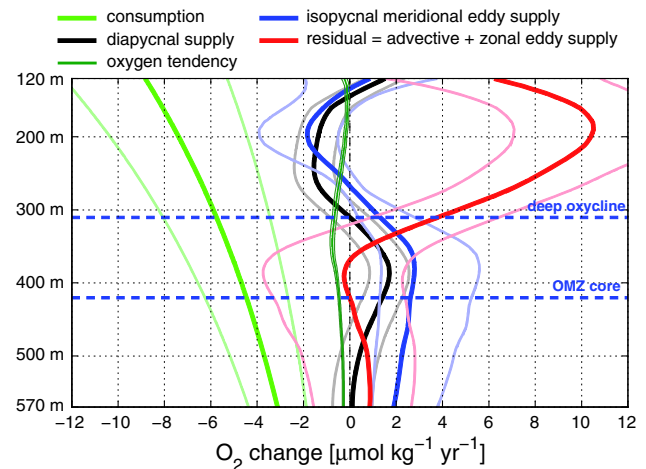


Fig. 14 Terms contributing to the oxygen budget (O_2 tendency = O_2 consumption + diapycnal O_2 supply + isopycnal meridional O_2 eddy supply + residual O_2 supply) in the Tropical North East Atlantic (latitudinal average between 6°N and 14°N, cf. *black dashed box* in Fig. 13) as a function of depth. The oxygen consumption profile (*green thick line*) was estimated by Karstensen et al. (2008). Diapycnal oxygen supply (*black thick line*) was estimated by Fischer et al. (2013). The isopycnal meridional eddy-driven oxygen supply (*blue thick line*) is from our study. Oxygen tendency was estimated as the difference of the apparent oxygen utilization (AOU) between periods 1999–2008 and 1972–1985 [data used from Brandt et al. (2010)]. The residual supply (*red thick line*) defines the ventilation through mean advection and zonal eddy diffusion. All error estimates are referred to a 95 % confidence [except the isopycnal meridional eddy supply, where the error was estimated from both the error of the oxygen curvature (95 % confidence) and the error of the eddy diffusivity (factor 2 assumed)]. *Horizontal dashed blue lines* mark the depths of the upper boundary (deep oxycline) and the core of the OMZ, that were estimated from the average oxygen profile between 6°N and 14°N

detailed description of the mean flow field is given e.g. by Stramma et al. (2008a) and Brandt et al. (2010)].

The oxygen variance (Fig. 1b) in regime 1 (6°S–4°N) shows a strong coherence (1) to the latitudinally banded structure of the mean zonal currents and (2) to locations with a strong mean isopycnal or diapycnal oxygen gradient. In case (1) oxygen variability can be caused by variability of the current strength, which leads to variability in the strength of zonal ventilation from the west (Brandt et al. 2008) or it can be caused by a meridional or vertical displacement of the high/low oxygen regions, which are generally associated with eastward/westward currents. In case (2) the extended Osborn–Cox model shows that mesoscale stirring/diapycnal mixing generates oxygen variance on isopycnal surfaces when acting on a mean isopycnal/diapycnal oxygen gradient. A quantification of the processes, mentioned in (1) and (2), that are responsible for the oxygen variability, cannot be made in the near-equatorial regime. Under such conditions it would be necessary to consider the full tracer variance equations [cf. (4.4), (4.5) in Ferrari and Polzin (2005)] with its divergent and

non-homogeneous terms, that are neglected when deriving the extended Osborn–Cox relation.

Nevertheless, the strong oxygen variance maximum at the equator at 300 m depth could be recently explained by Brandt et al. (2012). They show that most of the oxygen variability with a range of $\Delta O_2 = 60 \mu\text{mol kg}^{-1}$ is caused by equatorial deep jets having a dominant oscillation period at an interannual time scale of about 4.5 years.

In regime 2 (4°N – 14°N) strong oxygen variability occurred at shallow depths (100 m) over a wide meridional range as well as at intermediate depths (300–800 m). Oxygen variability at intermediate depths was enhanced at the boundaries of the OMZ following the $80 \mu\text{mol kg}^{-1}$ oxygen isoline. Due to a reduced mean flow below a depth of ~ 200 m, the oxygen variance has to be caused dominantly by mesoscale stirring (southern and upper OMZ boundary) and diapycnal mixing (upper OMZ boundary) of the mean oxygen field. Here, we have to assume that the effect of seasonal and longer-term variations of the mean flow field on the oxygen variance can be neglected against other terms. In such a regime, the total observed oxygen variance can be approximately considered as the equilibrium state between oxygen variance production and dissipation as described in the extended Osborn–Cox relation. However, in the present study the oxygen variance dissipation could not be determined in order to prove the validity of this relation.

The interior of the TNEA OMZ showed little oxygen variability. Due to the weak mean oxygen gradients, neither mesoscale stirring nor diapycnal mixing is able to generate much oxygen variability in this region.

The reason for the shallow oxygen variance maximum above 200 m (6°N – 14°N) could not be clarified. Stronger mean near-surface zonal currents as well as strong diapycnal oxygen gradients exist at this depth. For the same arguments as in regime 1 we assume that zonal current variability as well as diapycnal mixing are reasonable mechanisms that can cause this broad maximum.

The eddy-driven meridional oxygen flux is directed towards the center of the TNEA OMZ. Although the estimates from moored observations (time series of maximum 3 years length) at the southern OMZ boundary were hardly significant, the flux profiles agreed well with the diffusive flux parameterization. Rotational tracer fluxes (that have no contribution to a mean tracer budget) cannot be estimated, and thus not excluded, from a single mooring time series. However, we believe that they have only a minor contribution to the estimated oxygen fluxes, since mean currents are rather weak at least at depths below 200 m. At shallower depths (100–200 m) a stronger variability of the meridional oxygen fluxes from moored observations was found and it is likely that stronger currents at these depths lead to enhanced rotational tracer fluxes (Marshall and Shutts 1981; Eden

et al. 2007). A second reason for the higher variability is that the correlation of oxygen and velocity time series reflects a local estimate of the oxygen flux leading to a higher variability in regions with a strongly changing meridional oxygen gradient. Between 4°N and 6°N , the NECC advects oxygen-rich water from the western boundary eastward, at least during boreal summer (Stramma et al. 2008a). It is likely that the seasonal variability as well as a meridional meandering of the NECC/NEUC (Garzoli and Richardson 1989) causes a strong variability in strength and position of the meridional oxygen gradient leading to a higher variability of the meridional oxygen flux.

At the southern boundary of the OMZ (5°N , 23°W) we found a seasonal cycle of the turbulent meridional oxygen flux, which is of the same order of magnitude as the flux itself. The variability was strongest near the surface at depths of 100–300 m (not shown), but it was still evident at larger depths from 400 to 800 m (here, it was shown for 400 and 500 m). The calculation of annual harmonics of zonal velocity and oxygen from mooring time series at 5°N , 23°W and 500 m depth yielded an amplitude of about 1 cm s^{-1} and $6 \mu\text{mol kg}^{-1}$ with zonal velocity leading oxygen by about 2 months (not shown), which is in general agreement with zonal ventilation from the western boundary. Associated changes in strength and position of the meridional oxygen gradient might thus be responsible for the seasonal cycle of the turbulent meridional oxygen flux. However, a contribution from seasonal variations in the eddy diffusivity (e.g. due to a seasonal cycle in the strength of TIWs) cannot be excluded.

Moored observations at the southern boundary regime of the OMZ (5°N and 8°N) revealed pronounced fluctuations of meridional velocity at periods corresponding to mesoscale activity (larger than 30 days) and near-inertial oscillations (2–6 days). Spectra of oxygen fluctuations were observed with weaker energy maxima and a similarly weak energy minimum in between both time scales. In order to qualitatively describe the observed frequency spectra we refer to the theory of interior quasi-geostrophic turbulence²² which describes the wavenumber spectra of kinetic energy to follow a behavior $\sim k^{-3}$ in the submesoscale inertial range (Callies and Ferrari 2013). Variance spectra of a passive tracer classically roll off as $\sim k^{-1}$ due to a strong tracer filamentation, but Callies and Ferrari (2013) recently found that tracer variance is cascaded down with spectral slope $\sim k^{-2}$ for the interior ocean. By assuming frozen turbulence,²³ which scales frequency to

²² It is almost impossible to apply this theory to frequency spectra as acquired from moored observations (Ferrari and Wunsch 2010), thus our discussion is of qualitative nature.

²³ This is a very strong assumption and shall serve only as a qualitative description of the observed frequency spectra.

wavenumber by $f = Uk/(2\pi)$ (U being a characteristic background velocity), frequency spectra roll off as f^{-3} and f^{-2} for kinetic energy and a passive tracer, respectively.

Based on the above consideration, we defined the sub-mesoscale inertial range for the observed frequency spectra (Figs. 11a, b, 12a, b) between time scales of mesoscale variability and the inertial period (~ 10 – 30 days). For the considered frequency range, the slope of the meridional velocity PSD is indeed steeper compared to the oxygen PSD which is in qualitative agreement with the results obtained in wavenumber space (Callies and Ferrari 2013). The submesoscale inertial range ceases at frequencies close to the inertial period which is considered as an injection scale of kinetic energy for the internal wave spectrum as described within the Garrett-Munk model framework (Munk 1981).

The eddy-driven meridional oxygen supply is rather homogeneous in the interior of the OMZ (6°N – 14°N , 450 – 600 m) with an average value of about $2.1 \mu\text{mol kg}^{-1} \text{ year}^{-1}$ where the regime south/north of the OMZ core at 11°N is supplied through the southern/northern OMZ boundary.

At 100 m – 400 m, the eddy-driven meridional oxygen supply alternates in meridional bands of strong oxygen flux divergence (O_2 loss) and convergence (O_2 gain). Bands with a strong oxygen loss are centered at 4.5°S , equator, 5°N – 6°N and 9°N , which corresponds to locations of oxygen-rich eastward currents. Bands with a strong oxygen gain in between coincide with locations of either low-oxygen westward currents or bands with no or weak mean currents. Based on these conditions, the mesoscale eddy field redistributes oxygen-rich water from eastward currents and low-oxygen water from westward currents, which results in a total loss/gain of oxygen in eastward/westward currents. Locally, values $>10 \mu\text{mol kg}^{-1} \text{ year}^{-1}$ are reached and we assume that most of it is balanced by advection through the mean zonal currents. Nevertheless, Brandt et al. (2010) showed in a conceptual model study that the mean current field can be reasonably described by mean circulation cells. In such a cell, a recirculation takes place from an eastward current band into westward current bands north and south of it resulting also in oxygen fluxes due to mean meridional advection.

A refined picture of the oxygen budget in the TNEA was derived (Fig. 14). For the TNEA OMZ (here, an average over the depth range 350 m – 570 m was analyzed) it is composed as follows. Karstensen et al. (2008) found an average oxygen consumption of $-4.1 \mu\text{mol kg}^{-1} \text{ year}^{-1}$. Diapycnal mixing supplies the OMZ with about $0.9 \mu\text{mol kg}^{-1} \text{ year}^{-1}$ (Fischer et al. 2013), whereas meridional eddy fluxes ventilate the OMZ with about $2.4 \mu\text{mol kg}^{-1} \text{ year}^{-1}$. The oxygen tendency is about $-0.4 \mu\text{mol kg}^{-1} \text{ year}^{-1}$ [data used from Brandt et al. (2010)].

Thus, the residual oxygen supply required to balance all the other terms is $\sim 0.4 \mu\text{mol kg}^{-1} \text{ year}^{-1}$ (with high uncertainty). This residual supply splits into (1) an oxygen supply through mean advection and (2) an eddy-driven zonal oxygen supply. We expect the eddy-driven zonal oxygen supply to be an order of magnitude smaller than the eddy-driven meridional oxygen supply, since the zonal curvature of the mean isopycnal oxygen distribution is much smaller than the meridional curvature.²⁴ Consequently, the meridional oxygen flux due to mesoscale eddies is the dominant mechanism for the ventilation of the TNEA OMZ, which agrees with recent model studies on the large scale oxygen budget (Gnanadesikan et al. 2013; McCreary et al. 2013). A comparison with the total required oxygen supply ($-4.1 \mu\text{mol kg}^{-1} \text{ year}^{-1}$) shows that the eddy-driven meridional oxygen supply accounts for roughly 60 %, the diapycnal supply for about 20 % and the advective supply for <10 % of the total required oxygen supply at the depth range 350 – 570 m. The oxygen trend estimated by Stramma et al. (2008b) and Brandt et al. (2010) reveals that about 10 % of the consumed oxygen is not supplied by any of these ventilation processes.

The observed oxygen decrease over the last decades in the TNEA OMZ (Stramma et al. 2008b) reveals that some changes either in the ventilation or the oxygen consumption must have happened during this period. Brandt et al. (2010) suggested that a weakening of the nNECC, in particular at depth of the OMZ, could have contributed to such oxygen decrease. This might be corroborated by the shape of the oxygen tendency profile showing maximum oxygen decrease at about 340 m depth slightly below the deep oxycline. Such depth dependence would be in agreement with a general weakening and/or shallowing of the advective oxygen supply. Here we want to note only that the average oxygen tendency at depth of the OMZ is $-0.4 \mu\text{mol kg}^{-1} \text{ year}^{-1}$, which is a non-negligible term in the oxygen balance. It corresponds to about 10 % of the magnitude of the oxygen consumption, 20 % of the magnitude of the eddy-driven meridional oxygen supply, and about 45 % of the magnitude of the diapycnal oxygen supply. As an example, to close the oxygen budget just by an increase of the eddy-driven meridional oxygen flux, the oxygen curvature between northern and southern boundary of the OMZ (or the oxygen difference between OMZ core and its northern and southern boundary) would have to increase by 20 % when assuming no change in the eddy diffusivity K_e , which corresponds to a substantial deoxygenation in the core of the OMZ.

Above the OMZ in a depth range of 120 – 350 m meridional eddy fluxes and diapycnal mixing lead to a net

²⁴ The diffusive oxygen supply is the stronger the larger the curvature (2nd derivative) of the isopycnal oxygen distribution [cf. (16)].

loss of oxygen. The residual oxygen supply is largest in this depth range showing a maximum of $10 \mu\text{mol kg}^{-1} \text{ year}^{-1}$ at 200 m depth. Considering Fig. 13, this result can be the effect of an asymmetric average over meridional bands of strong oxygen flux divergence and convergence and we expect that a meridional average including latitudes further north ($>14^\circ\text{N}$) would reduce the strength of the residual. However, the essential mechanism responsible for the ventilation of this regime is the mean advection through the circulation cells associated with zonal jets, whereas the eddy diffusion leads to a meridional redistribution of oxygen between these jets. Hence, we expect a substantial contribution of the mean advection at this depth range and suspect that it supplies the OMZ at least down to 450 m corresponding to the maximum depth of the meridional bands of oxygen flux divergence and convergence.

Acknowledgments This study was supported by the German Science Foundation as part of the Sonderforschungsbereich 754 “Climate-Biogeochemistry Interactions in the Tropical Ocean”. We thank Marcus Dengler and Tim Fischer for helpful discussions, Sven-Helge Didwischus for post-processing of the velocity sections and Andreas Pinck for the development and the maintenance of the optode oxygen loggers.

Appendix 1: Estimate of the characteristic eddy velocity from ship sections (parameterization of the low pass filter)

As mentioned in Sect. 3.2, the velocity variability on the mesoscale cannot be estimated from repeat ship sections via time scale analysis. Here, we propose a simple parameterization to separate the variability on the mesoscale from short term variability, such as tidal and inertial oscillations. For this purpose, we use the velocity anomalies of the 5°N , 23°W mooring data. The basic idea is to calculate the magnitude (standard deviation) of the velocity fluctuations once with $(\sigma_{Lu} \hat{=} u_e$ and $\sigma_{Lv} \hat{=} v_e$, representing the mesoscale velocity fluctuations) and without $(\sigma_u$ and σ_v , representing the total velocity fluctuations) applying a low-pass filter L , where the cutoff frequency of the low-pass filter is chosen corresponding to a period of 10 days. Then, we do a polynomial fit of σ_u and σ_v against σ_{Lu} and σ_{Lv} to parameterize the effect of L , i.e.

$$\sigma_{Lu} = a_0 + a_1 \sigma_u + a_2 \sigma_u^2 + a_3 \sigma_u^3 \quad (19)$$

$$\sigma_{Lv} = a_0 + a_1 \sigma_v + a_2 \sigma_v^2 + a_3 \sigma_v^3. \quad (20)$$

The parameterization of the low-pass filter is based on the following assumptions: (1) The magnitude of the low-pass filtered velocity fluctuations (σ_{Lu} and σ_{Lv}) tends to zero, if σ_u and σ_v tend to zero. Thus, $a_0 = 0$. (2) Without loss of generality we assumed that the ratio of inertial and

tidal oscillations to the total velocity variability varies with the magnitude of the total velocity variability. Consequently, at least three degrees of freedom are necessary for this parameterization, where a_0 is already defined as 0. Nevertheless, we add another degree of freedom to reduce the residual of the fit (see Sect. 4.2 for results). The application of the polynomial fit (19) and (20) on the 5°N , 23°W mooring data is shown in Fig. 5 and yielded the following values for the polynomial coefficients: $a_1 = 0.15$, $a_2 = 0.11 (\text{m s}^{-1})^{-1}$, $a_3 = -5.2 \times 10^{-3} (\text{m s}^{-1})^{-2}$.

Appendix 2: Meridional oxygen flux using the correlation of velocity and oxygen time series

The total meridional oxygen flux at a given position is defined as

$$\mathcal{F} = \overline{vO_2} \quad (21)$$

where the overbar denotes the temporal average on a density surface over the recorded time series. We now use the Reynolds decomposition to separate the time series into a mean $(\overline{\cdot})$ and an anomaly $(\cdot)'$ on surfaces of potential density, i.e.

$$v(\sigma_\theta, t) = \overline{v}(\sigma_\theta) + v'(\sigma_\theta, t) \quad (22)$$

$$O_2(\sigma_\theta, t) = \overline{O_2}(\sigma_\theta) + O_2'(\sigma_\theta, t) \quad (23)$$

where $\overline{v'} = \overline{O_2'} = 0$. Applying (21)–(23) the flux on a density surface is then given by

$$\mathcal{F}(\sigma_\theta) = \underbrace{\overline{v(\sigma_\theta)} \overline{O_2(\sigma_\theta)}}_{\mathcal{F}(\sigma_\theta)} + \underbrace{\overline{v'(\sigma_\theta, t) O_2'(\sigma_\theta, t)}}_{\mathcal{F}'(\sigma_\theta)} \quad (24)$$

with the mean isopycnal oxygen flux $\mathcal{F}(\sigma_\theta)$ and the turbulent isopycnal oxygen flux $\mathcal{F}'(\sigma_\theta)$. The mean oxygen flux is highly uncertain (not shown), since the relative velocity error $\Delta v/\bar{v}$ is very large.²⁵ The mean oxygen flux due to a zonal mean flow was studied using a simple advection diffusion model in Brandt et al. (2010) and will not be considered here. Our main goal is the estimation of the eddy-driven oxygen flux and we therefore concentrate on the term $\mathcal{F}'(\sigma_\theta)$.

Oxygen time series were recorded on distinct depth levels (see Table 2). Due to density variability, (23) leads to gappy time series for a single density surface, which can cause large uncertainties for the results of (24). Alternatively, we define the turbulent lateral oxygen flux at the

²⁵ Based on repeat shipboard ADCP sections and moored ADCPs, the absolute value of the mean meridional velocity at 5°N , 23°W and 8°N , 23°W was estimated to $<1 \text{ cm s}^{-1}$. The measurement error (Sect. 2.1) is of the same order of magnitude ($<2 \text{ cm s}^{-1}$).

instrument depth z_I via a weighted average over density surfaces, which is given by

$$F'(z_I) = \frac{\sum_{i=1}^S n_i \mathcal{F}'(\sigma_{\theta i})}{\sum_{i=1}^S n_i}, \quad (25)$$

where n_i is the number of data points that were measured on the i th density surface during the mooring period and $\sum_{i=1}^S n_i = N$ is the total number of data points of the time series. The time average in (24) is defined by $\overline{(\cdot)} = \sum_{j=1}^n (\cdot)/n$ and (25) transforms to

$$\begin{aligned} F'(z_I) &= \frac{\sum_{i=1}^S n_i \left\{ \frac{1}{n_i} \sum_{j=1}^{n_i} v'_j(\sigma_{\theta i}) O'_{2j}(\sigma_{\theta i}) \right\}}{\sum_{i=1}^S n_i} \\ &= \frac{\sum_{i=1}^S \sum_{j=1}^{n_i} v'_j(\sigma_{\theta i}) O'_{2j}(\sigma_{\theta i})}{\sum_{i=1}^S n_i} \end{aligned} \quad (26)$$

The double summation over indices i and j is basically a sum over the whole time series and can be written as

$$F'(z_I) = \frac{\sum_{k=1}^N v'_k O'_{2k}}{N} \quad (27)$$

v'_k and O'_{2k} being the recorded time series of velocity and oxygen anomalies at the instrument depth z_I . $F'(z_I)$ is the turbulent meridional oxygen flux at the instrument depth z_I representing a weighted average over all isopycnal surfaces that were sampled by the instrument during the mooring period. The error for the turbulent meridional oxygen flux is estimated as the standard error of an arithmetic mean value, i.e.

$$\Delta F' = \frac{F'(z_I)}{\sqrt{n_f}} \quad (28)$$

where n_f represents the degrees of freedom of the time series. We estimated n_f from the autocorrelation function of the velocity time series as follows: the number m of correlated data points in the time series was calculated by testing the autocorrelation function of the meridional velocity against 0-coherence on a 95 % confidence level and assuming the statistics of a t-distribution for the correlation coefficient. The degrees of freedom were computed with the total number of data points N divided by the number of correlated data points m

$$n_f = \frac{N}{m}. \quad (29)$$

References

- AADI (2007) TD 218 operating manual oxygen optode 3830, 3835, 3930, 3975, 4130, 4175. Aanderaa Data Instruments. <http://www.aanderaa.com/>
- AADI (2009) TD 269 operating manual oxygen optode 4330, 4835. Aanderaa Data Instruments. <http://www.aanderaa.com/>
- Antonov JJ, Seidov D, Boyer TP, Locarnini RA, Mishonov AV, Garcia HE, Baranova OK, Zweng MM, Johnson DR (2010) World Ocean Atlas 2009, vol 2: salinity. In: Levitus S (ed) NOAA Atlas NESDIS 69, US Government Printing Office, Washington, DC, p 184
- Ascani F, Firing E, Dutrieux P, McCreary JP, Ishida A (2010) Deep equatorial ocean circulation induced by a forced-dissipated Yanai beam. *J Phys Oceanogr* 40(5):1118–1142. doi:10.1175/2010jpo4356.1
- Athie G, Marin F (2008) Cross-equatorial structure and temporal modulation of intraseasonal variability at the surface of the Tropical Atlantic Ocean. *J Geophys Res Oceans* 113(C8). doi:10.1029/2007jc004332
- Banyte D, Tanhua T, Visbeck M, Wallace DWR, Karstensen J, Krahmann G, Schneider A, Stramma L, Dengler M (2012) Diapycnal diffusivity at the upper boundary of the tropical North Atlantic oxygen minimum zone. *J Geophys Res Oceans* 117. doi:10.1029/2011jc007762
- Banyte D, Visbeck M, Tanhua T, Fischer T, Krahmann G, Karstensen J (2013) Lateral diffusivity from tracer release experiments in the tropical North Atlantic thermocline. *J Geophys Res Oceans* 118(5):2719–2733. doi:10.1002/jgrc.20211
- Bopp L, Le Quere C, Heimann M, Manning AC, Monfray P (2002) Climate-induced oceanic oxygen fluxes: implications for the contemporary carbon budget. *Glob Biogeochem Cycle* 16(2). doi:10.1029/2001gb001445
- Brandt P, Eden C (2005) Annual cycle and interannual variability of the mid-depth tropical Atlantic Ocean. *Deep Sea Res Part I Oceanogr Res Pap* 52(2):199–219. doi:10.1016/j.dsr.2004.03.011
- Brandt P, Schott FA, Provost C, Kartavtseff A, Hormann V, Bourles B, Fischer J (2006) Circulation in the central equatorial Atlantic: mean and intraseasonal to seasonal variability. *Geophys Res Lett* 33(7). doi:10.1029/2005gl025498
- Brandt P, Hormann V, Bourles B, Fischer J, Schott FA, Stramma L, Dengler M (2008) Oxygen tongues and zonal currents in the equatorial Atlantic. *J Geophys Res Oceans* 113(C4). doi:10.1029/2007jc004435
- Brandt P, Hormann V, Kortzinger A, Visbeck M, Krahmann G, Stramma L, Lumpkin R, Schmid C (2010) Changes in the ventilation of the oxygen minimum zone of the tropical North Atlantic. *J Phys Oceanogr* 40(8):1784–1801. doi:10.1175/2010jpo4301.1
- Brandt P, Greatbatch RJ, Claus M, Didwischus SH, Hormann V, Funk A, Hahn J, Krahmann G, Fischer J, Kortzinger A (2012) Ventilation of the equatorial Atlantic by the equatorial deep jets. *J Geophys Res Oceans* 117. doi:10.1029/2012jc008118
- Bunge L, Provost C, Hua BL, Kartavtseff A (2008) Variability at intermediate depths at the equator in the Atlantic ocean in 2000–2006: annual cycle, equatorial deep jets, and intraseasonal meridional velocity fluctuations. *J Phys Oceanogr* 38(8):1794–1806. doi:10.1175/2008jpo3781.1
- Callies J, Ferrari R (2013) Interpreting energy and tracer spectra of upper-ocean turbulence in the submesoscale range (1–200 km). *J Phys Oceanogr* 43(11):2456–2474. doi:10.1175/jpo-d-13-063.1
- De Szoeke RA, Bennett AF (1993) Microstructure fluxes across density surfaces. *J Phys Oceanogr* 23(10):2254–2264. doi:10.1175/1520-0485(1993)023<2254:mfads>2.0.co;2
- Eden C (2007) Eddy length scales in the North Atlantic Ocean. *J Geophys Res Oceans* 112(C6). doi:10.1029/2006jc003901
- Eden C, Greatbatch RJ (2008) Towards a mesoscale eddy closure. *Ocean Model* 20(3):223–239. doi:10.1016/j.ocemod.2007.09.002
- Eden C, Greatbatch RJ (2009) A diagnosis of isopycnal mixing by mesoscale eddies. *Ocean Model* 27(1–2):98–106. doi:10.1016/j.ocemod.2008.12.002

- Eden C, Greatbatch RJ, Olbers D (2007) Interpreting eddy fluxes. *J Phys Oceanogr* 37(5):1282–1296. doi:[10.1175/jpo3050.1](https://doi.org/10.1175/jpo3050.1)
- Eden C, Olbers D, Greatbatch RJ (2009) A generalized Osborn–Cox relation. *J Fluid Mech* 632:457–474. doi:[10.1017/s0022112009007484](https://doi.org/10.1017/s0022112009007484)
- Ferrari R, Polzin KL (2005) Finescale structure of the T–S relation in the eastern North Atlantic. *J Phys Oceanogr* 35(8):1437–1454. doi:[10.1175/jpo2763.1](https://doi.org/10.1175/jpo2763.1)
- Ferrari R, Wunsch C (2010) The distribution of eddy kinetic and potential energies in the global ocean. *Tellus Ser A Dyn Meteorol Oceanol* 62(2):92–108. doi:[10.1111/j.1600-0870.2009.00432.x](https://doi.org/10.1111/j.1600-0870.2009.00432.x)
- Fischer T, Banyte D, Brandt P, Dengler M, Krahmann G, Tanhua T, Visbeck M (2013) Diapycnal oxygen supply to the tropical North Atlantic oxygen minimum zone. *Biogeosciences* 10(7):5079–5093. doi:[10.5194/bg-10-5079-2013](https://doi.org/10.5194/bg-10-5079-2013)
- Funk A, Brandt P, Fischer T (2009) Eddy diffusivities estimated from observations in the Labrador Sea. *J Geophys Res Oceans* 114. doi:[10.1029/2008jc005098](https://doi.org/10.1029/2008jc005098)
- Garcia HE, Gordon LI (1992) Oxygen solubility in seawater—better fitting equations. *Limnol Oceanogr* 37(6):1307–1312
- Garcia HE, Locarnini RA, Boyer TP, Antonov JJ, Baranova OK, Zweng MM, Johnson DR (2010) World Ocean Atlas 2009, vol 3: dissolved oxygen, apparent oxygen utilization, and oxygen saturation. In: Levitus S (ed) NOAA Atlas NESDIS 70, US Government Printing Office, Washington, DC, p 344
- Garrett C (2001) Stirring and mixing: what are the rate controlling processes? In: Paper presented at the proceedings of the Aha Huliko’a winter workshop, University of Hawaii at Manoa
- Garzoli SL, Katz EJ (1983) The forced annual reversal of the Atlantic north equatorial countercurrent. *J Phys Oceanogr* 13(11):2082–2090. doi:[10.1175/1520-0485\(1983\)013<2082:tfarot>2.0.co;2](https://doi.org/10.1175/1520-0485(1983)013<2082:tfarot>2.0.co;2)
- Garzoli S, Richardson PL (1989) Low-frequency meandering of the Atlantic north equatorial countercurrent. *J Geophys Res Oceans* 94(C2):2079–2090. doi:[10.1029/JC094iC02p02079](https://doi.org/10.1029/JC094iC02p02079)
- Gent PR, McWilliams JC (1990) Isopycnal mixing in ocean circulation models. *J Phys Oceanogr* 20(1):150–155. doi:[10.1175/1520-0485\(1990\)020<0150:imioem>2.0.co;2](https://doi.org/10.1175/1520-0485(1990)020<0150:imioem>2.0.co;2)
- Getzlaff J, Dietze H (2013) Effects of increased isopycnal diffusivity mimicking the unresolved equatorial intermediate current system in an earth system climate model. *Geophys Res Lett* 40(10):2166–2170. doi:[10.1002/grl.50419](https://doi.org/10.1002/grl.50419)
- Gnanadesikan A, Bianchi D, Pradal MA (2013) Critical role for mesoscale eddy diffusion in supplying oxygen to hypoxic ocean waters. *Geophys Res Lett* 40(19):5194–5198. doi:[10.1002/grl.50998](https://doi.org/10.1002/grl.50998)
- Greatbatch RJ, Zhai XM, Eden C, Olbers D (2007) The possible role in the ocean heat budget of eddy-induced mixing due to air–sea interaction. *Geophys Res Lett* 34(7). doi:[10.1029/2007gl029533](https://doi.org/10.1029/2007gl029533)
- Kamenkovich I, Berloff P, Pedlosky J (2009) Anisotropic material transport by eddies and eddy-driven currents in a model of the North Atlantic. *J Phys Oceanogr* 39(12):3162–3175. doi:[10.1175/2009jpo4239.1](https://doi.org/10.1175/2009jpo4239.1)
- Karstensen J, Stramma L, Visbeck M (2008) Oxygen minimum zones in the eastern tropical Atlantic and Pacific oceans. *Prog Oceanogr* 77(4):331–350. doi:[10.1016/j.pocean.2007.05.009](https://doi.org/10.1016/j.pocean.2007.05.009)
- Keeling RF, Körtzinger A, Gruber N (2010) Ocean deoxygenation in a warming world. *Annual Rev Mar Sci* 2:199–229. doi:[10.1146/annurev.marine.010908.163855](https://doi.org/10.1146/annurev.marine.010908.163855)
- Lilly JM, Rhines PB, Schott F, Lavender K, Lazier J, Send U, D’Asaro E (2003) Observations of the Labrador Sea eddy field. *Prog Oceanogr* 59(1):75–176. doi:[10.1016/j.pocean.2003.08.013](https://doi.org/10.1016/j.pocean.2003.08.013)
- Locarnini RA, Mishonov AV, Antonov JJ, Boyer TP, Garcia HE, Baranova OK, Zweng MM, Johnson DR (2010) World Ocean Atlas 2009, vol 1: temperature. In: Levitus S (ed) NOAA Atlas NESDIS 68. US Government Printing Office, Washington, DC, p 184
- Luyten J, Pedlosky J, Stommel H (1983a) Climatic inferences from the ventilated thermocline. *Clim Chang* 5(2):183–191. doi:[10.1007/bf00141269](https://doi.org/10.1007/bf00141269)
- Luyten JR, Pedlosky J, Stommel H (1983b) The ventilated thermocline. *J Phys Oceanogr* 13(2):292–309. doi:[10.1175/1520-0485\(1983\)013<0292:tvt>2.0.co;2](https://doi.org/10.1175/1520-0485(1983)013<0292:tvt>2.0.co;2)
- Marshall J, Shutts G (1981) A note on rotational and divergent eddy fluxes. *J Phys Oceanogr* 11(12):1677–1680. doi:[10.1175/1520-0485\(1981\)011<1677:anorad>2.0.co;2](https://doi.org/10.1175/1520-0485(1981)011<1677:anorad>2.0.co;2)
- Matear RJ, Hirst AC (2003) Long-term changes in dissolved oxygen concentrations in the ocean caused by protracted global warming. *Glob Biogeochem Cycle* 17(4). doi:[10.1029/2002gb001997](https://doi.org/10.1029/2002gb001997)
- McCreary JP, Yu ZJ, Hood RR, Vinayachandran PN, Furue R, Ishida A, Richards KJ (2013) Dynamics of the Indian-Ocean oxygen minimum zones. *Prog Oceanogr* 112:15–37. doi:[10.1016/j.pocean.2013.03.002](https://doi.org/10.1016/j.pocean.2013.03.002)
- McDougall TJ (1987) Neutral surfaces. *J Phys Oceanogr* 17(11):1950–1964. doi:[10.1175/1520-0485\(1987\)017<1950:ns>2.0.co;2](https://doi.org/10.1175/1520-0485(1987)017<1950:ns>2.0.co;2)
- Meissner KJ, Galbraith ED, Volker C (2005) Denitrification under glacial and interglacial conditions: a physical approach. *Paleoceanography* 20(3). doi:[10.1029/2004pa001083](https://doi.org/10.1029/2004pa001083)
- Müller TJ, Siedler G (1992) Multi-year current time series in the eastern North Atlantic Ocean. *J Mar Res* 50(1):63–98
- Munk W (1981) Internal waves and small-scale processes. In: Warren BA, Wunsch C (eds) *Evolution of physical oceanography*. MIT Press, Cambridge, MA, pp 264–291
- Osborn TR, Cox CS (1972) Oceanic fine structure. *Geophys Fluid Dyn* 3(1):321–345. doi:[10.1080/03091927208236085](https://doi.org/10.1080/03091927208236085)
- Oschlies A, Schulz KG, Riebesell U, Schmittner A (2008) Simulated 21st century’s increase in oceanic suboxia by CO₂-enhanced biotic carbon export. *Glob Biogeochem Cycle* 22(4). doi:[10.1029/2007gb003147](https://doi.org/10.1029/2007gb003147)
- Stramma L, Huttel S, Schafstall J (2005) Water masses and currents in the upper tropical northeast Atlantic off northwest Africa. *J Geophys Res Oceans* 110(C12). doi:[10.1029/2005jc002939](https://doi.org/10.1029/2005jc002939)
- Stramma L, Brandt P, Schafstall J, Schott F, Fischer J, Kortzinger A (2008a) Oxygen minimum zone in the North Atlantic south and east of the Cape Verde Islands. *J Geophys Res Oceans* 113(C4). doi:[10.1029/2007jc004369](https://doi.org/10.1029/2007jc004369)
- Stramma L, Johnson GC, Sprintall J, Mohrholz V (2008b) Expanding oxygen-minimum zones in the tropical oceans. *Science* 320(5876):655–658. doi:[10.1126/science.1153847](https://doi.org/10.1126/science.1153847)
- Stramma L, Visbeck M, Brandt P, Tanhua T, Wallace D (2009) Deoxygenation in the oxygen minimum zone of the eastern tropical North Atlantic. *Geophys Res Lett* 36. doi:[10.1029/2009gl039593](https://doi.org/10.1029/2009gl039593)
- Stramma L, Oschlies A, Schmidt S (2012) Mismatch between observed and modeled trends in dissolved upper-ocean oxygen over the last 50 yr. *Biogeosciences* 9(10):4045–4057. doi:[10.5194/bg-9-4045-2012](https://doi.org/10.5194/bg-9-4045-2012)
- Uchida H, Kawano T, Kaneko I, Fukasawa M (2008) In situ calibration of optode-based oxygen sensors. *J Atmos Ocean Technol* 25(12):2271–2281. doi:[10.1175/2008jtecho549.1](https://doi.org/10.1175/2008jtecho549.1)
- Urbano DF, Jochum M, da Silveira ICA (2006) Rediscovering the second core of the Atlantic NECC. *Ocean Model* 12(1–2):1–15. doi:[10.1016/j.ocemod.2005.04.003](https://doi.org/10.1016/j.ocemod.2005.04.003)
- Vallis GK (2006) *Atmospheric and oceanic fluid dynamics*. Cambridge University Press, Cambridge
- von Schuckmann K, Brandt P, Eden C (2008) Generation of tropical instability waves in the Atlantic Ocean. *J Geophys Res Oceans* 113(C8). doi:[10.1029/2007jc004712](https://doi.org/10.1029/2007jc004712)
- Wunsch C (1999) Where do ocean eddy heat fluxes matter? *J Geophys Res Oceans* 104(C6):13235–13249. doi:[10.1029/1999jc000062](https://doi.org/10.1029/1999jc000062)
- Wyrki K (1962) The oxygen minima in relation to ocean circulation. *Deep Sea Res* 9(1):11–23. doi:[10.1016/0011-7471\(62\)90243-7](https://doi.org/10.1016/0011-7471(62)90243-7)